SPHGal: Smoothed Particle Hydrodynamics with improved accuracy for galaxy simulations

Chia-Yu Hu[1], Thorsten Naab[1], Stefanie Walch[2,1], Benjamin P. Moster[3,1], Ludwig Oser[4]

[1] *Max-Planck-Institut für Astrophysik, Karl-Schwarzschild Strasse 1, D-85740 Garching, Germany*
[2] *Physikalisches Institut der Universität zu Köln, Zülpicher Strasse 77, D-50937 Köln, Germany*
[3] *Institute of Astronomy, Madingley Road, Cambridge CB3 0HA, UK*
[4] *Department of Astronomy, Columbia University, New York, NY 10027, USA*

July 30, 2014

ABSTRACT

We present the smoothed-particle hydrodynamics implementation SPHGal, which combines some recently proposed improvements in GADGET. This includes a pressure-entropy formulation with a Wendland kernel, a higher order estimate of velocity gradients, a modified artificial viscosity switch with a modified strong limiter, and artificial conduction of thermal energy. With a series of idealized hydrodynamic tests we show that the pressure-entropy formulation is ideal for resolving fluid mixing at contact discontinuities but performs conspicuously worse at strong shocks due to the large entropy discontinuities. Including artificial conduction at shocks greatly improves the results. In simulations of Milky Way like disk galaxies a feedback-induced instability develops if too much artificial viscosity is introduced. Our modified artificial viscosity scheme prevents this instability and shows efficient shock capturing capability. We also investigate the star formation rate and the galactic outflow. The star formation rates vary slightly for different SPH schemes while the mass loading is sensitive to the SPH scheme and significantly reduced in our favored implementation. We compare the accretion behavior of the hot halo gas. The formation of cold blobs, an artifact of simple SPH implementations, can be eliminated efficiently with proper fluid mixing, either by conduction and/or by using a pressure-entropy formulation.

Key words: methods: numerical, galaxies: ISM, galaxies: intergalactic medium, galaxies: evolution, galaxies: spiral

1 INTRODUCTION

Smoothed-particle hydrodynamics (SPH) is a numerical method for solving fluid equations in a Lagrangian fashion (Lucy 1977; Gingold & Monaghan 1977). It has found a widespread use in a variety of astrophysical problems (e.g. Springel 2010b; Price 2012). The success of SPH lies in the exact conservation of physical properties and the adaptive resolution that traces mass. In addition, the Lagrangian nature ensures Galilean invariance by construction. Practically, the method is also straightforward to be incorporated with tree-based gravity solvers and is intuitive for including subresolution physics.

However, recent studies (e.g. Agertz et al. 2007; Springel 2010a) have shown that standard SPH has serious difficulties to properly model fluid mixing. Its accuracy is therefore compromised when modeling the interstellar medium (Heitsch, Naab & Walch 2011) and galaxy formation (Sijacki et al. 2012; Nelson et al. 2013). The problem originates from a numerical artifact at contact discontinuities (often referred to as the spurious 'surface tension'). One solution proposed by Price (2008) is to include artificial conduction to alleviate

such artifacts, though with the potential issue of being overly diffusive. Therefore, several conduction switches have been suggested to reduce unwanted conduction away from the entropy discontinuities (Read & Hayfield 2012; Valdarnini 2012). An alternative solution to the problem is to modify the definition of density so that the pressure is smoothed by construction (Ritchie & Thomas 2001; Read, Hayfield & Agertz 2010; Saitoh & Makino 2013; Hopkins 2013). To its advantage no extra dissipation is needed, the entropy is still conserved and the contact discontinuities remain sharp.

Another criticism of SPH is its slow convergence rate. SPH is second order accurate only in the continuous limit. When the fluid is discretized into SPH particles, there exists a zeroth order error in the equation of motion (Read, Hayfield & Agertz 2010; Price 2012). This error can be reduced by using more neighboring particles within the kernel. However, the commonly used cubic spline kernel is subject to the pairing instability when too many neighboring particles are used (Price 2012). Read, Hayfield & Agertz (2010) introduced a new kernel function without an inflection point to prevent the pairing instability. Dehnen & Aly (2012) pro-

posed to use the Wendland C^4 kernel and demonstrated its stability despite having an inflection point. These studies demonstrate a significantly improved convergence rate compared to the standard SPH with only a minor impact on the computational efficiency.

With these recent developments, many authors have updated the existing 'problematic' implementations to improve the accuracy and ensure the scientific credibility of their simulations. Power, Read & Hobbs (2013) presented simulations of the formation of an idealized (non-radiative) galaxy cluster using three different methods: the traditional SPH, their improved implementation (SPHS) and an adaptive mesh refinement (AMR) code (see also Hubber, Falle & Goodwin (2013) for a recent AMR/SPH comparison). They find that SPHS and AMR are in excellent agreement while the traditional SPH shows a different behavior. On the other hand, Hopkins et al. (2013) presented cosmological simulations including more complicated physical processes and found very little difference between their improved SPH implementation and the traditional SPH. Feng et al. (2013) simulated the accretion of supermassive black holes at high redshifts and found that their improved SPH gives rise to slightly faster black hole growth, while the star formation is unaffected.

In this paper, we incorporate the most important improvements into the hydrodynamic code GADGET-3 (Springel 2005) and test different implementations with idealized hydrodynamic tests. We use the pressure-entropy formulation presented in Hopkins (2013) and the Wendland C^4 kernel with 200 neighboring particles. The artificial viscosity scheme we adopt resembles Cullen & Dehnen (2010) but with a slight modification in its functional form. We also include artificial conduction similar to Read & Hayfield (2012). However, the major role of conduction in our case is to help capture shocks. We show that the pressure-entropy formulation performs poorly in the Sedov explosion test without artificial conduction. At contact discontinuities, however, the pressure-entropy formulation alone is able to properly model the fluid mixing. We therefore suppress the artificial conduction in shear flows.

We also investigate the properties of different SPH schemes in a more complex three dimensional simulation of isolated disk galaxy models with gas, star formation and supernova feedback. Standard SPH implementations can result in the formation of artificial large, kpc-sized, holes which are then sheared apart. If too much viscosity is introduced the gaseous disks become unstable and the simulations fail dramatically. Fortunately, such instabilities can be avoided with a slight modification of the viscosity limiter.

We present a modified SPH version, which we term SPHGal, that passes the Gresho, Sod shock tube, Sedov explosion, 'square', Keplerian ring, Kelvin-Helmholtz and 'blob' test and also performs well in more realistic galaxy simulations. The strengths and limitations of this implementation are discussed in detail.

This paper is organized as follows: in Section 2 we present the details of our SPH implementation. The results of the idealized hydrodynamic tests are shown in Section 3 with detailed discussions of the pros and cons of different implementations. In Section 4 we present simulations of isolated disk galaxy models and show the properties of the gaseous disk, the star formation rate and galactic outflow, and the accretion behaviors. We summarize and discuss our work in Section 5.

2 HYDRODYNAMIC METHOD

2.1 Improving the convergence rate

In SPH, the pressure force in the equation of motion is not guaranteed to vanish in a medium of constant pressure, which is referred to as the "E0 error" in Read, Hayfield & Agertz (2010). This residual force vanishes only when SPH particles are distributed regularly within the kernel. The convergence scaling of SPH is therefore, in general, worse than $O(h^2)$. Although this error can be factored out to obtain a locally more precise form of the pressure gradient, the inevitable trade-off is the violation of exact momentum conservation and losing the capability of particle reordering (Price 2012), making it less favorable in practice. One straightforward way of reducing the E0 error is to increase the particle number in the kernel so that the integration accuracy is improved. However, the commonly used cubic spline kernel is subject to the pairing instability when using too many neighboring particles (Price 2012). Alternative kernel functions immune to pairing instability have been proposed (Read, Hayfield & Agertz 2010; Dehnen & Aly 2012). Here we adopt the Wendland C^4 kernel as in Dehnen & Aly (2012) and use 200 neighboring particles as our default setup.

2.2 Pressure-entropy formulation

It has been widely recognized that the standard SPH does not properly model fluid mixing at contact discontinuities (Ritchie & Thomas 2001; Agertz et al. 2007). The problem is that while the density is smoothed on a kernel scale at the boundaries, the entropy remains sharply discontinuous, leading to a so-called "pressure blip" which acts as a spurious surface tension, suppressing fluid instabilities. More than ten years ago Ritchie & Thomas (2001) derived an alternative density estimate which can avoid this numerical artifact. Read, Hayfield & Agertz (2010) proposed a generalized discretization of the Euler equation where the density estimate in Ritchie & Thomas (2001) is a special case. Saitoh & Makino (2013) explored a similar idea and derived a density-independent SPH formulation by choosing a different volume element. Hopkins (2013) took into account the variation of the smoothing length (the "grad-h" term) based on a Lagrangian approach, making the new formulation exactly conservative, which is important for modeling shocks.

We adopt the pressure-entropy (PE) formulation derived in Hopkins (2013), where pressure and entropy are the primary variables. The pressure is estimated by

$$\widehat{P}_i = \left[\sum_{j=1}^{N} m_j A_j^{1/\gamma} W_{ij}(h_j) \right]^{\gamma}, \qquad (1)$$

where N is the number of neighboring particles in the kernel, m_j is the particle mass, W_{ij} is the smoothing kernel, h_j is the smoothing length, A_j is the entropy function and γ is the polytropic index such that $P = A\rho^{\gamma}$. The equation of

motion is

$$\frac{d\mathbf{v}_i}{dt} = -\sum_{j=1}^{N} m_j (A_i A_j)^{1/\gamma}$$
$$\times \left[\frac{f_{ij}\widehat{P}_i}{\widehat{P}_i^{2/\gamma}} \nabla_i W_{ij}(h_i) + \frac{f_{ji}\widehat{P}_j}{\widehat{P}_j^{2/\gamma}} \nabla_i W_{ij}(h_j) \right], \tag{2}$$

where

$$f_{ij} = 1 - \left(\frac{h_i}{3A_j^{1/\gamma} m_j \widehat{n}_i} \frac{\partial \widehat{P}_i^{1/\gamma}}{\partial h_i} \right) \left[1 + \frac{h_i}{3\widehat{n}_i} \frac{\partial \widehat{n}_i}{\partial h_i} \right]^{-1} \tag{3}$$

is the correction term for variable smoothing lengths and

$$\widehat{n}_i = \sum_{j=1}^{N} W_{ij} \tag{4}$$

is the number density estimate. The entropy is given by the initial conditions and requires no evolution in the dissipation-less case. Other thermodynamic variables (e.g. density) can be derived from the estimated pressure and entropy.

The advantage of such a formulation is that the pressure is smoothed by construction and therefore has no spurious jump at contact discontinuities. Fluid instabilities can thus develop without being numerically suppressed, and the hot and cold regions of the fluid then mix with each other within a few instability time-scales. However, this formulation is not without its weaknesses. In many astrophysical situations, especially at strong shocks, the variation in entropy from one particle to another is usually several orders of magnitude larger than in density. A particle with high entropy would then have an overwhelming weight even if it is located at the edge of the kernel. The pressure estimate, in such cases, would be much noisier or even biased compared to the standard density-entropy (DE) SPH formulation. **This can be seen most clearly by linear error analysis (Read, Hayfield & Agertz 2010). Assuming the smoothing length is constant, Equation (2) can be written as**

$$\frac{d\mathbf{v}_i}{dt} = -\sum_{j=1}^{N} \frac{m_j}{\rho_i \rho_j} \left[\frac{\rho_j}{\rho_i} \frac{A_j^{1/\gamma}}{A_i^{1/\gamma}} P_i + \frac{\rho_i}{\rho_j} \frac{A_i^{1/\gamma}}{A_j^{1/\gamma}} P_j \right] \nabla_i W_{ij}$$
$$= -\frac{P_i}{\rho_i} \sum_{j=1}^{N} \frac{m_j}{\rho_j} \left[\frac{\rho_j}{\rho_i} \frac{A_j^{1/\gamma}}{A_i^{1/\gamma}} + \frac{\rho_i}{\rho_j} \frac{A_i^{1/\gamma}}{A_j^{1/\gamma}} \right] \nabla_i W_{ij} \tag{5}$$
$$- \frac{\nabla P_i}{\rho_i} \sum_{j=1}^{N} \frac{m_j}{\rho_j} \frac{\rho_i}{\rho_j} \frac{A_i^{1/\gamma}}{A_j^{1/\gamma}} (\mathbf{x}_j - \mathbf{x}_i) \otimes \nabla_i W_{ij} + O(h^2),$$

where we have used $P_j = P_i + \nabla P_i \cdot (\mathbf{x}_j - \mathbf{x}_i) + O(h^2)$. **Therefore, for the equation of motion to be second order accurate, the following two conditions have to be satisfied:**

$$\mathbf{E}_i \equiv \sum_{j=1}^{N} \frac{m_j}{\rho_j} \left[\frac{\rho_j}{\rho_i} \frac{A_j^{1/\gamma}}{A_i^{1/\gamma}} + \frac{\rho_i}{\rho_j} \frac{A_i^{1/\gamma}}{A_j^{1/\gamma}} \right] \nabla_i W_{ij} = \mathbf{0},$$
$$\tag{6}$$
$$\mathbf{V}_i \equiv \sum_{j=1}^{N} \frac{m_j}{\rho_j} \frac{\rho_i}{\rho_j} \frac{A_i^{1/\gamma}}{A_j^{1/\gamma}} (\mathbf{x}_j - \mathbf{x}_i) \otimes \nabla_i W_{ij} = \mathbf{I},$$

where $\mathbf{E}_i$ **is the dominate error (E0 error). At contact discontinuities,** $\rho_j A_j^{1/\gamma} \rho_i^{-1} A_i^{-1/\gamma} \approx 1$ **across the interface, which minimizes** $\mathbf{E}_i$ **as** $\nabla_i W_{ij}$ **is an odd**

function. However, at strong shocks, $\rho_j A_j^{1/\gamma} \rho_i^{-1} A_i^{-1/\gamma}$ **can deviate from unity by several orders of magnitude due to the large entropy jump. Furthermore, as both density and entropy are larger in the post-shock regions, their effects in** $\mathbf{E}_i$ **in general do not cancel out.**

2.3 Artificial viscosity

We implement artificial viscosity (AV) as in Monaghan (1997) and Springel (2005):

$$\left(\frac{d\mathbf{v}_i}{dt} \right)_{\text{vis}} = -\sum_{j=1}^{N} m_j \Pi_{ij} \nabla_i \overline{W}_{ij}, \tag{7}$$

where $\overline{W}_{ij}$ represents the arithmetic average of $W_{ij}(h_i)$ and $W_{ij}(h_j)$, and

$$\Pi_{ij} = \begin{cases} -\frac{1}{2} \frac{\bar{\alpha}_{ij} v_{\text{sig}}}{\bar{\rho}_{ij}} \omega_{ij} & \text{if } \omega_{ij} < 0 \\ 0 & \text{otherwise}, \end{cases} \tag{8}$$

where $\omega_{ij} = \mathbf{v}_{ij} \cdot \widehat{x}_{ij}$ is the approaching velocity of particle pairs, $v_{\text{sig}} = c_i + c_j - 3\omega_{ij}$ is the signal speed, $\bar{\rho}_{ij}$ is the arithmetic average of ρ_i and ρ_j, and $\bar{\alpha}_{ij}$ is the arithmetic average of α_i and α_j. The viscosity also generates entropy at a rate

$$\frac{dA_i}{dt} = \frac{1}{2} \frac{\gamma - 1}{\rho_i^{\gamma-1}} \sum_{j=1}^{N} m_j \Pi_{ij} \mathbf{v}_{ij} \cdot \nabla_i \overline{W}_{ij}. \tag{9}$$

This commonly adopted form of AV is devised to conserve momentum. However, it does not distinguish between bulk and shear viscosity since the viscous term Π_{ij} involves only the relative velocity of particle pairs, irrespective of the local velocity gradient. This can lead to excessive viscosity especially in shear flows, generating spurious angular momentum transport in a rotating disk. A common reduction scheme is to include a limiter that suppresses AV wherever the vorticity dominates over the velocity divergence (Balsara 1989, 1995, see also Dolag et al. 2005; Nelson, Wetzstein & Naab 2009). More recently, Morris & Monaghan (1997) proposed a variable viscosity coefficient α_i for each SPH particle. The basic idea is that α_i should increase only when a converging flow is detected ($\nabla \cdot \mathbf{v} < 0$), and decays to a minimum value afterwards in a few sound-crossing times. This "switch" efficiently suppresses unwanted viscosity away from shocks and has also been implemented in other SPH codes (e.g Wetzstein et al. 2009).

Cullen & Dehnen (2010) further improved this method in several ways. They set α_i immediately to a desired value based on a shock indicator to ensure that α_i rises rapidly enough wherever needed. They also used the time derivative of velocity divergence as a shock indicator to detect shocks in advance. Finally, they implemented a more precise estimate of the velocity gradient to prevent falsely triggered AV. Based on these principles, they proposed an AV scheme as follows: a limiter similar to the the Balsara switch is defined as

$$\xi_i = \frac{|2(1 - R_i)^4 \nabla \cdot \mathbf{v}_i|^2}{|2(1 - R_i)^4 \nabla \cdot \mathbf{v}_i|^2 + \mathbf{S}_i^2}, \tag{10}$$

where $\mathbf{S}_i = \sqrt{\mathbf{S}_{\alpha\beta} \mathbf{S}_{\alpha\beta}}$ is the Frobenius norm of the shear

tensor and

$$R_i = \frac{1}{\rho_i} \sum_j \text{sign}(\nabla \cdot \mathbf{v}) m_j W_{ij}. \tag{11}$$

The shock indicator is defined as

$$S_i = \xi_i \max(0, -\dot{\nabla} \cdot \mathbf{v}_i) \tag{12}$$

and the target value of the viscosity coefficient is

$$\alpha_{\text{tar},i} = \alpha_{\max} \frac{h_i^2 S_i}{h_i^2 S_i + v_{\text{dec},i}^2}, \tag{13}$$

where $v_{\text{dec},i}$ is the decay speed

$$v_{\text{dec},i} = \max_{\mathbf{x}_{ij} \leqslant h_i} (\bar{c}_{ij} - \min(0, \mathbf{v_{ij}} \cdot \widehat{\mathbf{x}_{ij}})). \tag{14}$$

The true viscosity coefficient of each particle evolves as

$$\alpha_i = \begin{cases} \alpha_{\text{tar},i} & \text{if } \alpha_i \leqslant \alpha_{\text{tar},i} \\ [\alpha_{\text{tar},i} + (\alpha_i - \alpha_{\text{tar},i}) \exp(-\text{d}t/\tau_i)] & \text{if } \alpha_i > \alpha_{\text{tar},i}, \end{cases} \tag{15}$$

where $\text{d}t$ is the time step and $\tau_i = 10 h_i / v_{\text{dec}}$ is the decay time. One characteristic of this scheme is that the limiter ξ_i in Equation (10) puts a relatively stronger weight on the velocity divergence than on the shear. Furthermore, the target value of the viscosity coefficient $\alpha_{\text{tar},i}$ may approach the maximum value $\alpha_{\max}$ if $h_i^2 S_i \gg v_{\text{dec},i}^2$ even when the limiter ξ_i is small. Therefore, in the case where both significant shocks and shear flows are involved, the effect of the limiter is weakened. We will therefore refer to this scheme as artificial viscosity with a 'weak limiter'.

We have modified the above functional form so that the effect of the viscosity limiter is stronger. This is to avoid too much viscosity when both shocks and shear flows are present . We will come back to this in more detail in Section 4.2 where we discuss the three-dimensional modeling of a disk galaxy. We adopt a slightly modified form of α_i while still following the same principles. We define the target value of the viscosity coefficient as

$$\alpha_{\text{tar},i} = \alpha_{\max} \frac{h_i^2 S_i}{h_i^2 S_i + c_i^2}, \tag{16}$$

where $S_i = \max(0, -\dot{\nabla} \cdot \mathbf{v}_i)$ is the shock indicator. The true viscosity coefficient of each particle evolves as

$$\alpha_i = \begin{cases} \xi_i \ \alpha_{\text{tar},i} & \text{if } \alpha_i \leqslant \alpha_{\text{tar},i} \\ \xi_i \left[\alpha_{\text{tar},i} + (\alpha_i - \alpha_{\text{tar},i}) \exp(-\text{d}t/\tau_i)\right] & \text{if } \alpha_i > \alpha_{\text{tar},i}, \end{cases} \tag{17}$$

where $\text{d}t$ is the time step and $\tau_i = 10 h_i / v_{\text{sig}}$ is the decay time with the decay speed

$$v_{\text{dec}} = \max_{\mathbf{x}_{ij} \leqslant h_i} (\bar{c}_{ij} - \min(0, \mathbf{v_{ij}} \cdot \widehat{\mathbf{x}_{ij}})), \tag{18}$$

and ξ_i is a limiter similar to the Balsara switch but in a quadratic form

$$\xi_i = \frac{|\nabla \cdot \mathbf{v}_i|^2}{|\nabla \cdot \mathbf{v}_i|^2 + |\nabla \times \mathbf{v}_i|^2 + 0.0001(c_i/h_i)^2}. \tag{19}$$

We use the same higher order velocity gradient estimate as Cullen & Dehnen (2010) to prevent falsely triggered AV. With a functional form as in Equation (16) AV is suppressed in a subsonic converging flow and rises up to a maximum value $\alpha_{\max}$ when the converging flow becomes supersonic. The major difference of this scheme from the weak-limiter scheme is that the limiter ξ_i is placed such that $\alpha_i \leqslant \xi_i \alpha_{\max}$

always holds. In addition, the limiter in Equation (19) puts equal weights to the velocity divergence and the vorticity. We adopt this scheme as our fiducial AV scheme and refer to it as artificial viscosity with a 'strong limiter'.

There is one subtlety in Equations (8) and (9) regarding the choice of ρ_i. In the PE formulation, the density can be estimated either by $\rho_i^e = (\widehat{P}_i/A_i)^{1/\gamma}$ (the "entropy-weighted" density), or by the traditional definition $\rho_i = \sum m_j W_{ij}$ (the "mass-weighted" density). We find the latter gives more accurate results in the case of strong shocks due to the large entropy jumps. Therefore, we use the traditional estimate whenever we need the density information. This includes radiative cooling, the conversion between entropy and internal energy, and the gradient estimate in Equations (20) and (21).

2.4   Artificial conduction

We include the artificial conduction (AC) of thermal energy similar to Read & Hayfield (2012), which explicitly conserves the total energy within the kernel:

$$\frac{\text{d}u_i}{\text{d}t} = \sum_{j=1}^{N} \bar{\alpha}_{ij}^d v_{\text{sig}} L_{ij}^p m_j \frac{u_i - u_j}{\bar{\rho}_{ij}} \widehat{x}_{ij} \cdot \nabla_i \overline{W}_{ij}, \tag{20}$$

where $v_{\text{sig}} = (c_i + c_j - 3\omega_{ij})$ and $L_{ij}^p = |P_i - P_j|/(P_i + P_j)$ is the pressure limiter proposed by Read & Hayfield (2012). In the continuous limit, Equation (20) recovers the thermal conduction equation $\text{d}u/\text{d}t = \eta \nabla^2 u$ with a thermal conductivity, $\eta = \alpha_{ij}^d v_{\text{sig}} L_{ij}^p x_{ij}/2$, scaling with the local resolution $x_{ij} \lesssim h$.

Although the artificial conduction may be interpreted as the turbulent mixing at sub-resolution scales (Wadsley, Veeravalli & Couchman 2008), the motivation here is purely numerical. As pointed out in Price (2008), just like momentum is smoothed by AV, the thermal energy (or entropy) should also be smoothed so that it remains differentiable everywhere. In the DE formulation of SPH, the presence of AC mitigates the problematic pressure blip at contact discontinuities. In the PE formulation the pressure is smoothed at contact discontinuities by construction, which seems to imply that the AC becomes redundant. However, the AC is still desirable (perhaps even necessary) in the PE formulation, not at contact discontinuities, but at strong shocks where the entropy jumps tend to be several orders of magnitude. The pressure estimate would be very noisy if there were no conduction to smooth out these entropy jumps.

To reduce artificial conduction away from entropy discontinuities, we use a conduction switch similar to the AV switch. We define an entropy jump indicator as the Laplacian of thermal energy in the form of Brookshaw (1985)

$$\nabla^2 u_i = 2 \sum_{j=1}^{N} m_j \frac{u_i - u_j}{\rho_j} \frac{\nabla_i W_{ij}}{|\mathbf{x}_{ij}|} \tag{21}$$

and a target conduction coefficient

$$\alpha_{\text{tar},i}^d = \alpha_{\max}^d \frac{|\nabla^2 u_i|}{|\nabla^2 u_i| + u_i/h_i^2}. \tag{22}$$

The true conduction coefficient evolves as

$$\alpha_i^d = \begin{cases} \xi_i \ \alpha_{\text{tar},i}^d & \text{if } \alpha_i^d \leqslant \alpha_{\text{tar},i}^d \\ \xi_i \left[\alpha_{\text{tar},i}^d + (\alpha_i^d - \alpha_{\text{tar},i}^d) \exp(-\text{d}t/\tau_i^d)\right] & \text{if } \alpha_i^d > \alpha_{\text{tar},i}^d, \end{cases} \tag{23}$$

where $\tau_i^d = 2h_i/v_{\text{dec}}$ is the decay time and ξ_i is the limiter defined in Equation (19) which suppresses the AC at shear flows. The limiter ξ_i here also guarantees that there will be no AC in a self-gravitating system under hydrostatic equilibrium as $\nabla \cdot \mathbf{v} = 0$ in such case.

2.5 Timestep limiter

As Saitoh & Makino (2009) pointed out, when modeling strong shocks, the adaptive time step scheme in SPH requires an additional constraint: the neighboring particles should have similar time steps comparable within a factor of a few. We set the factor to be 4 as our default choice. On top of that, Durier & Dalla Vecchia (2012) further pointed out that when feedback energy (thermal or kinetic alike) is injected, an inactive particle should shorten its time step and become active immediately. This is to ensure that ambient particles react to the explosion correctly and do not remain inactive when a shock is approaching. We activate the inactive particles right after they receive feedback energy.

3 HYDRODYNAMIC TESTS

3.1 Naming convention

We investigate different SPH schemes and their performance in the test problems. For simplicity, we assign an acronym to a specific SPH scheme (e.g. 'pe-avsl-ac', our fiducial scheme). The first segment indicates the adopted SPH formulation: 'pe' and 'de' are the pressure-entropy formulation and density-entropy formulation, respectively. The second segment indicates the AV scheme. For example, 'avB' is a constant AV with a Balsara switch, 'avwl' is AV with a weak-limiter, and 'avsl' is AV with a strong-limiter (see Section 2.3). If AC is included, we add another segment 'ac'. Finally, 'erho' uses the entropy-weighted density in the dissipation terms (AV and AC), and 'lvg' indicates the use of the lower order velocity gradient estimator. Table 1 summarizes all the SPH schemes investigated in this paper. The maximum value of the AV (and AC if applicable) coefficient is set to unity in all cases. We also set a minimum value for the AV coefficient to 0.1 in order to maintain particle order. Unless otherwise specified, we use the Wendland C^4 kernel with 200 neighboring particles.

3.2 Gresho vortex

The initial condition of the Gresho vortex test (Gresho & Chan 1990; Springel 2010b) consists of a two-dimensional differentially rotating vortex. The velocity and pressure profiles are as follows:

$$v_\phi(R) = \begin{cases} 5R & \text{for } 0 \leqslant R < 0.2, \\ 2 - 5R & \text{for } 0.2 \leqslant R < 0.4, \\ 0 & \text{for } R \geqslant 0.4; \end{cases} \quad (24)$$

$$P(R) = \begin{cases} 5 + 12.5R^2 & \text{for } 0 \leqslant R < 0.2, \\ 9 + 12.5R^2 & \\ -20R + 4\ln(5R) & \text{for } 0.2 \leqslant R < 0.4, \\ 3 + 4\ln 2 & \text{for } R \geqslant 0.4, \end{cases} \quad (25)$$
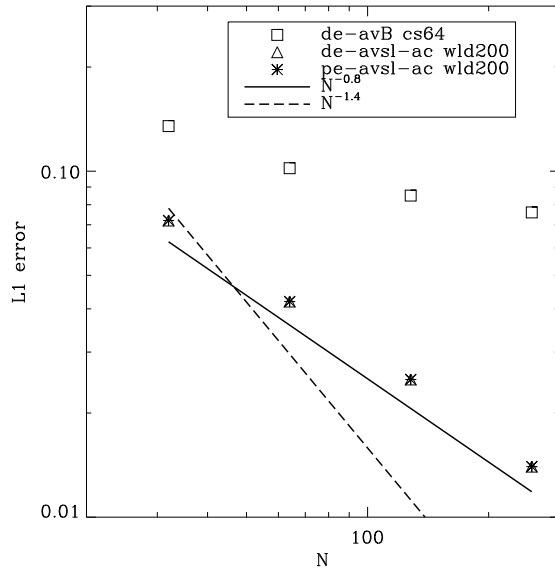
Figure 1. Convergence rate (L1 error vs. particle number) for the standard Gresho test at t = 1. The DE formulation with the standard cubic spline and 64 neighbors (cs64, open squares) has the worst convergence properties. The use of the Wendland C^4 kernel with 200 neighbors (wld200) improves convergence significantly (L1 $\propto N^{-0.8}$). The PE formulation (asterisks) and the DE formulation (triangles) give almost identical results. The dashed line (L1 $\propto N^{-1.4}$) is the convergence rate found with the moving mesh code AREPO (Springel 2010a).

where R is the radius. The density is constant $\rho = 1$ everywhere. We set up a slab in a close-packing lattice with an equivalent one-dimensional resolution N. The pressure profile is devised to balance the centrifugal force, which makes the system time-independent.

Fig. 1 shows the convergence rate (the L1 error) [1] of different SPH schemes. Due to the use of the Wendland C^4 kernel the convergence rate ($\propto N^{-0.8}$) is significantly improved (see Read & Hayfield (2012); Dehnen & Aly (2012) for a more detailed analysis) compared to the traditional SPH using cubic spline (see e.g. Kawata et al. 2013) with only 64 neighbors, though still lower than for moving mesh methods (e.g. $\propto N^{-1.4}$ found in Springel 2010a). [2] The DE and PE formulations give almost exactly the same results. This is not surprising as both density and pressure are continuous in this test and the two formulations are equally accurate.

Recently, Miczek (2013) presented a more general form of the standard Gresho problem which allows for changing the maximum Mach number of the system to study the behavior of grid-based methods in the low Mach number

---

[1] We follow Springel (2010b) and define the L1 error as the arithmetic average of the difference between the bin-averaged particle velocity and the analytic solution. The bin size we use is 0.01.

[2] One way to achieve a convergence rate $\propto N^{-1.4}$ for SPH, as shown in Read & Hayfield (2012), is to factor out the E0 error. However, such a scheme violates momentum conservation and performs poorly at strong shocks, making it less favorable in most of applications.

Table 1. Naming convention of different SPH schemes. The maximum value of the AV (and AC if applicable) coefficient is set to be 1 in all cases. We also set a minimum value for the AV coefficient of 0.1 to retain the particle order. Our favored and fiducial SPH scheme is 'pe-avsl-ac'.

Name	SPH formulation	artificial viscosity (AV)	artificial conduction (AC)	comments
de-avB	density-entropy	const. AV with Balsara switch	no	
de-avB-lvg	density-entropy	const. AV with Balsara switch	no	lower order velocity gradients
de-avsl	density-entropy	strong limiter	no	
de-avsl-ac	density-entropy	strong limiter	yes	
de-avwl	density-entropy	weak limiter	no	
de-avwl-ac	density-entropy	weak limiter	yes	
pe-avB	pressure-entropy	const. AV with Balsara switch	no	
pe-avsl	pressure-entropy	strong limiter	no	
pe-avsl-ac	pressure-entropy	strong limiter	yes	our fiducial choice
pe-avsl-ac-lvg	pressure-entropy	strong limiter	yes	lower order velocity gradients
pe-avwl	pressure-entropy	weak limiter	no	
pe-avwl-ac	pressure-entropy	weak limiter	yes	
pe-avsl-ac-erho	pressure-entropy	strong limiter	yes	use ρ^e in the dissipation terms

regime. While the density and velocity profiles remain unchanged, the pressure is modified as

$$
P(R) = \begin{cases}
P_0 + 12.5R^2 & \text{for } 0 \leqslant R < 0.2, \\
P_0 + 12.5R^2 + 4 \\
\quad -20R + 4\ln(5R) & \text{for } 0.2 \leqslant R < 0.4, \\
P_0 - 2 + 4\ln 2 & \text{for } R \geqslant 0.4,
\end{cases}
\tag{26}
$$

where $P_0 = (\gamma M^2)^{-1}$, and M is the maximum Mach number of the system. Note that this is merely a constant shift with respect to Equation (25). Therefore, the pressure gradient force does not change and still balances the centrifugal force. For $M = \sqrt{3/25} \approx 0.3$ it recovers the original Gresho problem. We now can investigate the performance of our fiducial SPH scheme (PE formulation with AC) in the low Mach number regime. Fig. 2 shows the results with different Mach number M with 1D resolution $N = 256$. The times are in code units and are proportional to the sound-crossing time for a given Mach number. The $M = 0.3$ case (corresponds to the standard Gresho test) in panel (a) is recovered nicely, though the systematically biased values at the discontinuities ($R = 0.2$ and $R = 0.4$) are still unavoidable. However, as the Mach number decreases, the scatter becomes more severe and the radial-binned mean values start to deviate from the analytic expectation. This is especially notable in the region of rigid-body rotation ($R < 0.2$). At lower Mach numbers the viscous force become stronger due to a higher sound speed. Therefore, even though the AV coefficient is maintained at a minimum value, the viscous effect is still conspicuous, leading to a spurious transportation of angular momentum. In addition, the fluctuations due to the E0 error are also more severe for higher sound speeds, which explains the scatter.

One plausible 'solution' is to remove the lower limit of the AV coefficient to reduce the viscous effects completely. In Fig. 3 we repeat the same tests but set $\alpha_{\min} = 0$. The viscosity is then only triggered by our AV switch. Unfortunately, the radially binned mean values are improved only modestly (slightly higher peak values) compared to Fig. 2 while the scatter increases significantly. The particle fluctuation caused by the E0 error is much more severe without the minimum viscosity. Such fluctuations in turn triggers AV

which then still leads to the deviation of the mean values. The effort of reducing the spurious transportation of angular momentum is hence in vain. We therefore use a minimum viscosity as our default choice.

In summary, due to the E0 error, it remains challenging to model highly subsonic shear flows ($M \leqslant 0.05$) even with our favored SPH scheme. This is in agreement with the results of Bauer & Springel (2012) who points out that the traditional SPH scheme yields problematic results in subsonic turbulence. This seems to be an intrinsic issue of SPH as the E0 error can only be reduced by using larger number of neighboring particles if the conservation properties are kept (Price 2012; Dehnen & Aly 2012).

3.3 Sod shock tube

In this section we present results from a shock tube test (Sod 1978) to assess the accuracy of the schemes for weak shocks. This standard test consists of two fluids that are initially stationary with moderate discontinuities in both density and pressure at the interface, producing three characteristic waves, namely the shock, the contact discontinuity, and the rarefaction wave, respectively. We set the initial density $\rho_l = 1$ and pressure $P_l = 1$ on the left-hand side, and $\rho_r = 0.125$ and $P_r = 0.05$ on the right-hand side, which makes the shock slightly supersonic (with a Mach number M $\approx$ 1.5). We set up a 3D tube with the total length $L = 1$ in a close-packing lattice with effectively 600 particles along the tube. The polytropic index is $\gamma = 5/3$. We do not initialize the AV coefficient to its maximum at the interface. Fig. 4 shows the result of the shock tube test at t = 0.1 with our fiducial SPH scheme ('pe-avsl-ac'). Both the density and pressure profiles are in good agreement with the analytic predictions. The locations of the three characteristic waves are correctly modeled. There are however some oscillations in the velocity profile in the post-shock region which probably indicates too little viscosity. This error should be acceptable as long as the average value still agrees with the analytic solution.

We further investigate the convergence rate of the velocity profile in Fig. 5. Following Read & Hayfield (2012),
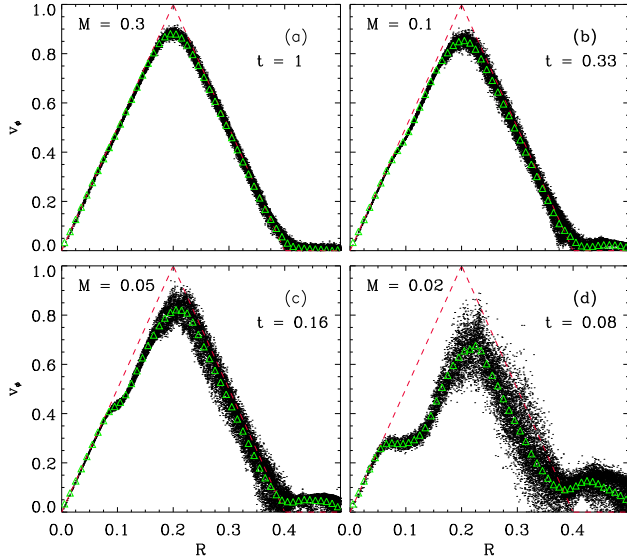
Figure 2. The velocity profile in the Gresho test with Mach number $M = 0.3$ (a), 0.1 (b), 0.05 (c), 0.02 (d), using our fiducial SPH implementation ('pe-avsl-ac'). The 1D resolution is $N = 256$. The time is proportional to the sound-crossing time. Only randomly drawn one per cent of the particles are shown. A lower limit of the AV coefficient $\alpha_{\min} = 0.1$ is used. The analytic solution is shown by the dashed red lines. The green triangles are the radial-binned mean values of v_ϕ. As the Mach number decreases, the velocity profiles start to deviate from the analytic solution the scatter increases.
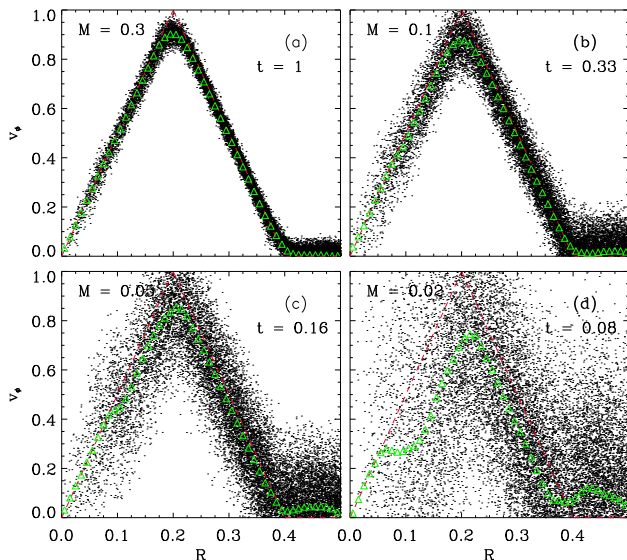
Figure 3. Same as Fig. 2 but with no lower limit to the AV coefficient. The mean values (green triangles) are improved only moderately while the scatter increases significantly.

we define the L1 error as

$$L1 = \frac{1}{N_b} \sum_i^{N_b} |\bar{v}_{x,i} - \bar{v}_x(x_i)| \qquad (27)$$

where N_b is the number of bins, $\bar{v}_{x,i}$ is the mean value of the particle velocity in the x-direction within bin i, and $\bar{v}_x(x_i)$ is
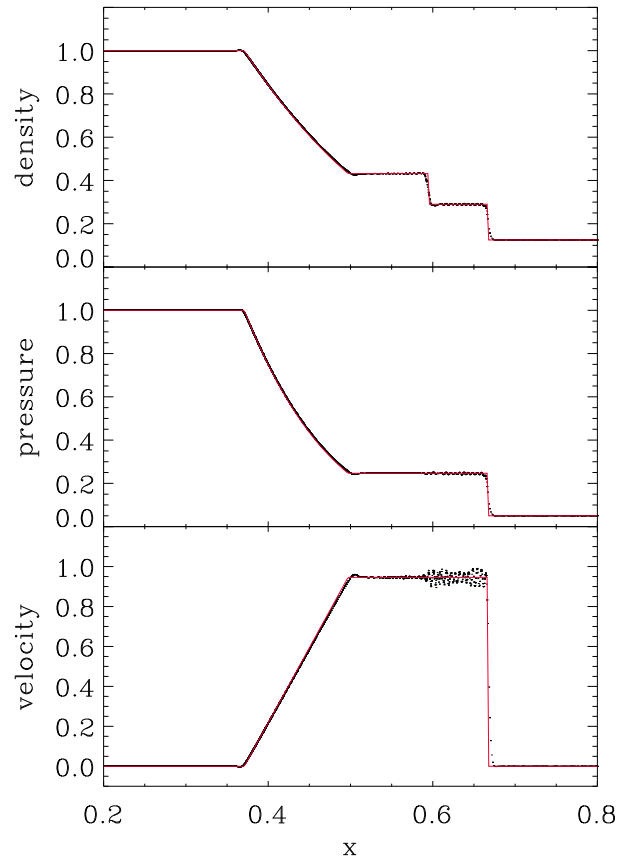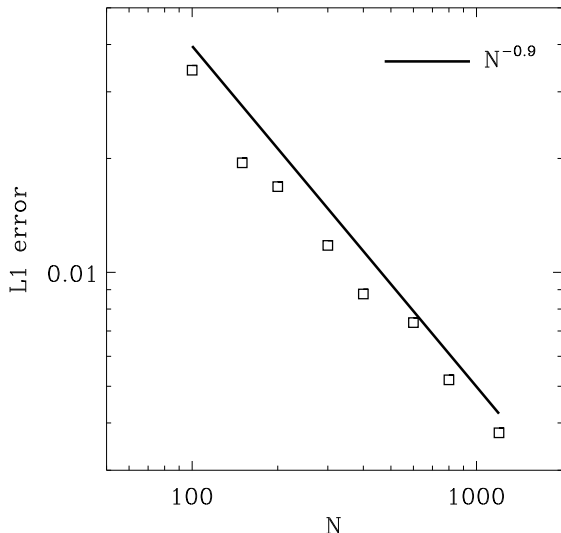

Figure 4. Shock tube test at $t = 0.1$, using our fiducial SPH ('pe-avsl-ac'). The density and pressure (top and middle panels) are in good agreement with the analytic prediction (red curves), while the velocity profile (bottom panel) shows weak oscillations in the post-shock region. Overall our fiducial scheme passes this test very well.

the mean analytic solution within bin i. We set a binsize of 0.005 and exclude the bins without particles. This binsize is small enough to capture the post-shock oscillations even in our highest resolution. We find the convergence rate close to $L1 \propto N^{-0.9}$, which is in agreement with Springel (2010b); Read & Hayfield (2012). As discussed in Springel (2010b), the accuracy of the scheme is limited to first order due to the error at the discontinuity.

3.4 Sedov explosion

The Sedov explosion (Sedov 1959) is an ideal test to evaluate the shock capturing capability of the code under extreme entropy contrasts. We set up a three-dimensional cube with 128^3 particles in a glass-like distribution. The initial density is constant at $\rho = 1.24 \times 10^7 M_\odot \mathrm{kpc}^{-3}$ ($n_H \approx 0.5 \mathrm{cm}^{-3}$) and the temperature is $T \approx 6.5$ K. The central 64 particles are then injected uniformly with a thermal energy of $E = 6.78 \times 10^{53}$ ergs, which results in a top-hat profile with a huge entropy contrast of 3×10^6. This corresponds to a Mach number $M \approx 1000$. We set the polytropic index to $\gamma = 5/3$ which represents the non-radiative phase of a Sedov blast
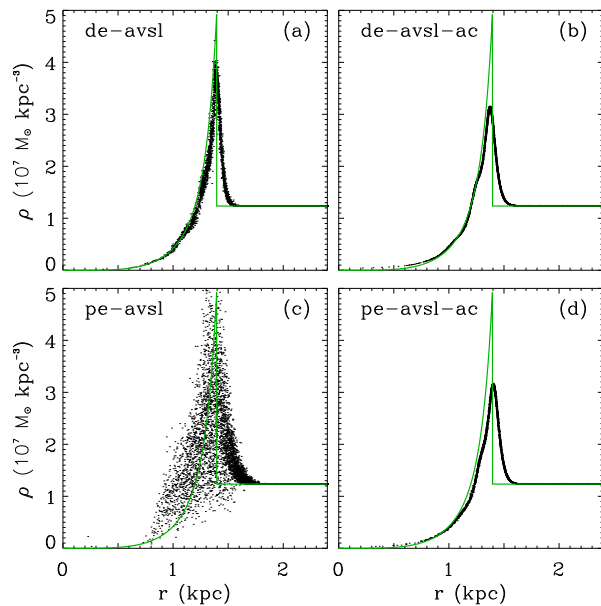
Figure 5. The convergence rate of the shock tube test at t = 0.1, using our fiducial SPH ('pe-avsl-ac'). The convergence rate is close to $L1 \propto N^{-0.9}$, close to the optimal rate of N^{-1} (see also Springel 2010b).

Figure 6. Density profile for a Sedov explosion after t = 30 Myr (showing only two per cent of randomly drawn particles). *Panel (a):* DE formulation without AC. *Panel (b):* DE formulation with AC. *Panel (c):* PE formulation without AC. *Panel (d):* PE formulation with AC. The green curves are the analytic solution. Without AC, the profile matches the analytic solution reasonably well (despite some scatter) using the DE formulation. On the other hand, using the PE formulation without AC the profile is very much dominated by noise. Including AC improves the results dramatically for both formulations (b and d).

wave (e.g. Ostriker & McKee 1988). This is a standard setup for testing a very strong shock (e.g. Hopkins 2013).

Fig. 6 shows the density profiles at t = 30 Myr using the DE and PE formulation, respectively. We plot two per cent of randomly drawn particles instead of radial binned values to indicate the scatter. For the DE formulation, the density profile agrees with the analytic solution quite well, though without AC (a) the scatter is higher. This is due to the sharp entropy discontinuity in the initial conditions. Once we include AC (b), the scatter is reduced significantly. This is in agreement with results presented in Read & Hayfield (2012).

For the PE formulation the situation becomes worse since the pressure estimate is entropy-weighted. Without AC (Fig. 6, panel c), particles penetrate the shock front anisotropically and eventually the noise dominates. This can in principle be improved by increasing the maximum value of the AV coefficient. **Indeed, Saitoh & Makino (2013) and Hopkins (2013) reported reasonably well results of a similar test without AC but using a much higher AV coefficient.** However, we find that including the AC (d) already significantly reduces the scatter. More importantly, for a reason that will be explained in Section 4.2, we try to avoid too much AV. The AC softens entropy jumps at the shock front and makes the entropy more continuous within the kernel. The resulting density profile and its scatter is as good as using the DE formulation with AC. We therefore consider AC a necessary ingredient in the PE formulation when strong shocks are involved. This is especially true for the disk simulations in Section 4 since our cooling implementation allows gas to cool down to a few hundred Kelvin instead of 10^4 K and the entropy contrast is usually much larger.

As discussed in Section 2.3, the density can be defined in two different ways for the PE formulation: as a mass-weighted density or a entropy-weighted density. In Fig. 7, panel (a), we show the two density estimates for the same simulation. At the shock (~ 1.2 kpc) the two densities agree well with each other. However, the entropy-weighted density has a "bump" ahead of the shock front. This bump can be understood as follows: in the Sedov test the entropy is discontinuous but the pressure is smoothed. Therefore, the entropy-weighted density $\rho_i^e = (\widehat{P}_i/A_i)^{1/\gamma}$ would be over/under-estimated in the pre/post-shock regions, biasing the result. Since the entropy jump is several orders of magnitude, the bias in the pre-shock region is much more severe and manifests itself as a bump. This is very similar to the "pressure blip" problem in the DE formulation. Both stem from the fact that one variable (density or pressure) is being smoothed while the other (entropy) remains sharply discontinuous.

In Fig. 7, panel (b), we further compare to a simulation using the entropy weighted density in the dissipation terms (AV and AC). Here the shock front falls notably behind. This can be understood as the result of the spurious pre-shock bump. In the pre-shock region the artificial viscosity is switched on, converting kinetic energy into thermal energy. However, the over-estimated density causes the entropy to be under-estimated in Equation (9). As such, the shock loses part of its driving force as if some energy has been lost or radiated away, and thus propagates slower. As shown in Fig. 7, panels (c) and (d), the AV and AC are both efficiently
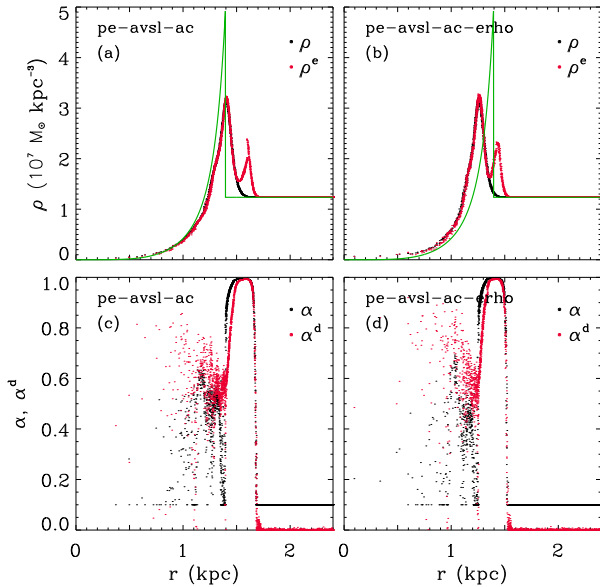
Figure 7. Density profiles and the distributions of the AV and AC coefficients at t = 30 Myr, using different definitions of density in the dissipation terms (showing only two per cent of randomly drawn particles). *Panel (a):* density profile using mass-weighting in the dissipation terms. Black dots and red dots are the mass-weighted and entropy-weighted densities, respectively. The green curve is the analytic solution. The peak position matches the analytic solution. A pre-shock density bump can been seen in the entropy-weighted density. *Panel (b):* same as (a) but using the entropy-weighted density in the dissipation terms. The peak falls behind the analytic solution. *Panel (c):* distribution of the AV (black dots) and AC (red dots) coefficients corresponding to (a). *Panel (d):* distribution of AV and AC coefficients corresponding to model (b).

Figure 8. Radial profile of velocity (a), temperature (b), divergence and curl of velocity (c), and pressure (d). All panels are generated with our fiducial SPH scheme ('pe-avsl-ac'). Only two per cent of randomly drawn particles are shown. The results are in good agreement with the analytic solution (green curves).

switched on right before the shock arrives. There are a few oscillations in the post-shock region as a result of the post-shock ringing and the limiter in Equation (19).
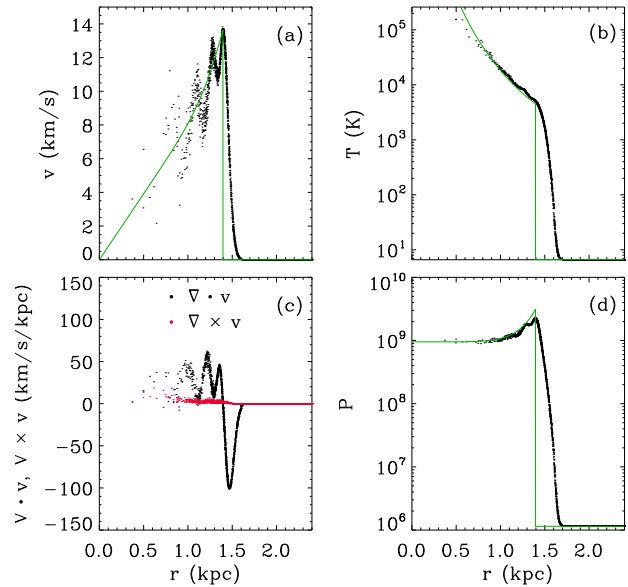
Fig. 8 shows the radial profile of velocity, temperature, and pressure for our fiducial model as well as the analytic solutions. Here, the post-shock ringing can be seen most clearly in the velocity profile and is unfortunately difficult to avoid in our implementation. The radial profile of the velocity divergence and curl shows that the former always dominates over the latter and the particle order in the post-shock region is kept reasonably well.

3.5 Keplerian ring

In this section we discuss results for a Keplerian ring test similar to Cartwright, Stamatellos & Whitworth (2009); Cullen & Dehnen (2010). We set up a two dimensional ring with a Gaussian surface density profile

$$\Sigma(r) = \frac{1}{m} \exp\left[-\frac{(r - r_0)^2}{2\sigma^2}\right], \qquad (28)$$

where m is the total mass of the ring, r_0 is the radius of the peak surface density, and σ is the width of the ring. We set $r_0 = 10$ and $\sigma = 1.25$. The ring is subject to the gravity of a point mass $M \gg m$ located at $r = 0$. The self-gravity of

the ring is neglected and we set $GM = 1000$, where G is the gravitational constant. The initial condition is set up with 9987 particles using the method presented in Cartwright, Stamatellos & Whitworth (2009) which generates a lattice-like particle distribution with concentric rings.

The rotation velocity of the ring follows a Keplerian velocity profile $v_\phi(r) = \sqrt{GM/r}$ and the rotation period at r_0 is therefore $T = 2\pi$. The sound speed of the ring, $c_s = 0.01 \ll v_\phi$, ensures that inviscid hydrodynamical processes only set in after several periods of rotation as discussed in Cullen & Dehnen (2010). The AV can be falsely triggered by a poor estimate of velocity gradients and then a viscous instability develops quickly, breaking the ring structure. In this test we do not use a minimum value of AV since even a small viscosity would lead to the instability. Because of the low sound speed, a small perturbation in velocity could be supersonic leading to shocks heating up the ring. This mostly starts from the inner edge of the ring where differential rotation is most prominent. In the absence of AV, the system is in equilibrium and should remain stable over several periods of rotation. Since the system is isothermal, the AC would not be triggered and can be neglected for this test.

Fig. 9 shows the results with different SPH schemes at the time (in code units) after which the ring structure breaks up. The standard Balsara switch (panel a) is too viscous and the instability sets in very quickly after one and a half rotation periods ($T = 2\pi$). Using our fiducial scheme but without the higher order estimate of velocity gradients (panel b) only delays the instability for less than one rotation period. Adopting the higher order velocity gradient estimator (Cullen & Dehnen 2010) greatly improves the situation.
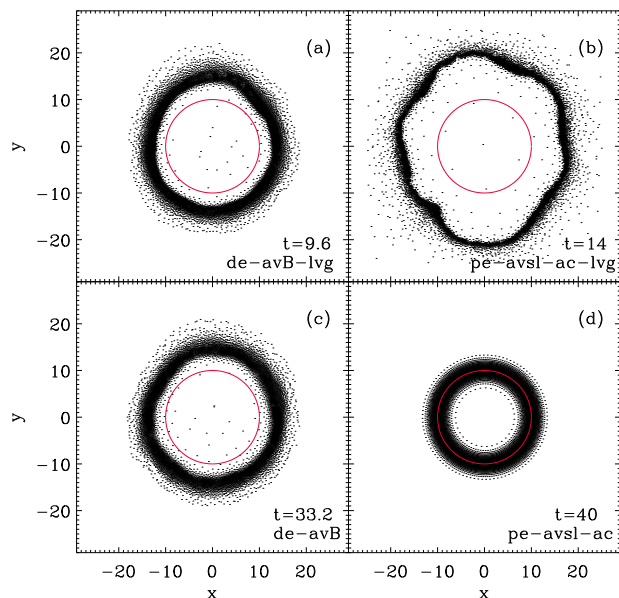
Figure 9. Two dimensional ring with a radial Gaussian density profile in Keplerian rotation at the time (in code units) when the ring structure breaks up. No lower limit of AV is used in this test. One rotation takes $T = 2\pi$. *Panel (a):* DE-formulation with Balsara switch, using lower order velocity gradients. *Panel (b):* PE-formulation with AC, using lower order velocity gradients. *Panel (c):* DE-formulation with Balsara switch, using higher order velocity gradients. *Panel (d):* PE-formulation with AC using higher order velocity gradients. Using higher order velocity gradients prevents falsely triggered AV (Cullen & Dehnen 2010) and therefore the ring remains stable for more than five rotation periods. The red solid rings indicate the location of the initial peak density.

Even with the Balsara switch that is usually considered to be too viscous, the system is able to evolve for about five periods before the instability sets in (panel b). With our fiducial scheme the AV is further reduced, and the system remains stable during the whole simulation time (t=40), very similar to the implementation presented in Cullen & Dehnen (2010).

3.6 Hydrostatic equilibrium test

In this section we present results from a hydrostatic equilibrium test similar to Saitoh & Makino (2013); Hopkins (2013) to examine spurious surface tension at contact discontinuities. We set up a two dimensional square $0 \leqslant x < 1$ and $0 \leqslant y < 1$ with periodic boundary conditions, filled up with a background fluid of uniform density $\rho = 7/4$. A slightly denser fluid of uniform density $\rho = 7$ is embedded in the central region where $0.25 \leqslant x < 0.75$ and $0.25 \leqslant y < 0.75$. We use $256 \times 256 \times 3$ particles in the background region and 512×512 in the central region, both in a cubic lattice configuration. All particles have the same mass. The pressure $P = 3.75$ is constant in both fluids. Fig. 10 shows the results for different SPH schemes after following the evolution of the system up to $t = 3$ (in code units). Initially the central fluid forms a perfect square. It has been shown that the square evolves into a circle due to spurious surface ten-
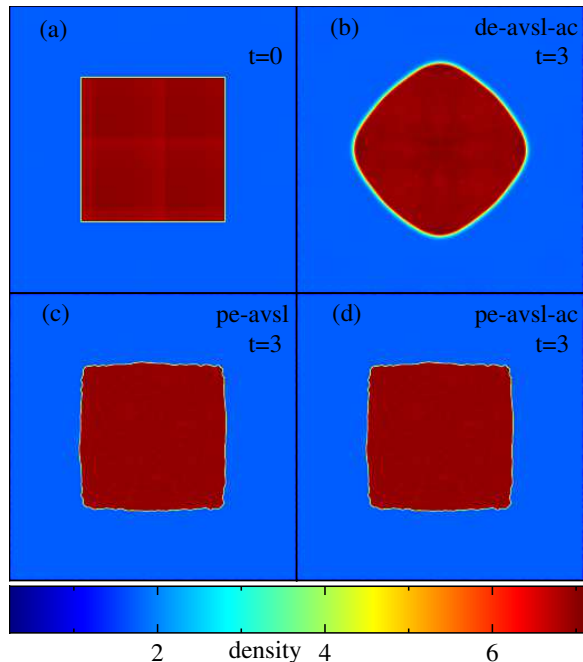
Figure 10. Density distribution for a square in hydrostatic equilibrium. *Panel (a):* initial condition. *Panel (b):* DE-formulation with AC at t = 3. *Panel (c):* PE-formulation without AC at t = 3. *Panel (d):* PE-formulation with AC at t = 3. The DE-formulation leads to deformation of the square even with AC. With PE-formulation the surface tension is absent right from the beginning and therefore the square retains its original shape.

sion in standard SPH implementations (Saitoh & Makino 2013; Hopkins 2013). Somehow surprisingly, it also deforms significantly with the DE-scheme and AC. This is probably due to the inertia exerted by the spurious surface tension in the initial conditions. Using the PE-formulation with or without AC the square retains its original shape (as demonstrated in Saitoh & Makino 2013; Hopkins 2013), although there are some small fluctuations at the boundaries because of the E0-error force. In the PE-formulation, the spurious surface tension is absent right from the beginning.

3.7 Kelvin-Helmholtz instability

The Kelvin-Helmholtz (KH) instability develops at contact discontinuities of shear flows and is an important mechanism for the onset of fluid turbulence. The inaccuracy of standard SPH in this test and the solutions to it have been well studied in the literature (e.g. Agertz et al. 2007; Price 2008; Junk et al. 2010; Valdarnini 2012; Kawata et al. 2013; Read & Hayfield 2012; Saitoh & Makino 2013; Hopkins 2013). Here we simply show the results with our fiducial scheme. The initial condition we set up is identical to Read & Hayfield (2012). The computational domain is a periodic slab of $256 \times 256 \times 16$ kpc. We use 774144, 2359296, and 5304748 equal-mass particles in a cubic lattice for density contrast of 2, 8, and 20, respectively. The fluid is divided into three (the top, middle and bottom) parts, which are in pressure equilibrium. The middle layer has a density $\rho_1 = 313$ $M_\odot/kpc^3$ and temperature $T_1 = 10^7$ K. The top and bottom layer have a density $\rho_2 = \chi\rho_1$ and temperature $T_2 = T_1/\chi$ K

where χ is the density contrast. The shear flow is set up such that the central fluid travels at $v_x = 40$ km/s while the upper and lower fluid travel at $v_x = -40$ km/s. A sinusoidal velocity perturbation in y direction of $\delta v_y = 4$ km/s with the wavelength $\lambda = 128$ kpc is applied to trigger the instability. The instability is expected to develop within a few Kelvin-Helmholtz time scales

$$\tau_{\mathrm{KH}} \equiv \frac{(1+\chi)\lambda}{(\chi)^{1/2}v}, \qquad (29)$$

where $v = 80$ km/s is the relative shear velocity at the interface. Fig. 11 shows the density contours at t = 1, 1.5, 2 and 3 τ_{KH} (from left to right) for a density contrast of $\chi = 2$ (top row), $\chi = 8$ (middle row), and $\chi = 20$ (bottom row). The KH instability develops in qualitative agreement with Read & Hayfield (2012) and Hopkins (2013). Note that the PE formulation itself is already capable of resolving the KH instability and the AC here is suppressed by the limiter in Equation (19) to avoid unnecessary dissipation. However, for higher density contrasts (20:1) there are some small-scale fluctuations at the boundaries due to the E0 error force and the system becomes more diffusive.
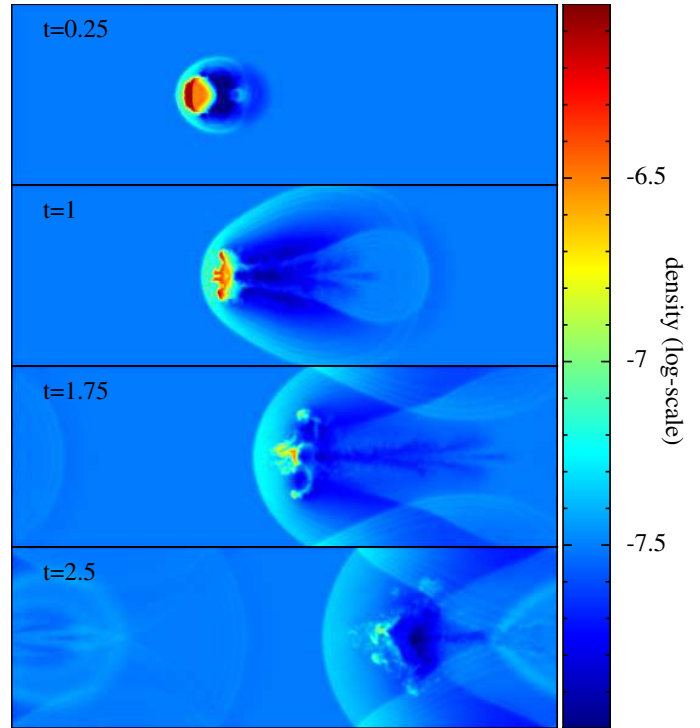
3.8 Blob test

The blob test (Agertz et al. 2007) is a complicated problem which involves several important physical processes. In this test, a spherical cloud of radius R_{cl} travels with Mach number $M = 2.7$ in an ambient medium that is 10 times hotter and 10 times less dense. We use the same initial conditions [3] as presented in Read, Hayfield & Agertz (2010). The computational domain is a tube with a size of $10 \times 10 \times 30$ in units of the cloud radius, with periodic boundary conditions. The particle number is 9641651 and all particles have the same mass. Spherical harmonics are used to initialize the perturbations of the cloud in order to trigger the instabilities. Although no analytic solution exists for such problem, the qualitative behavior can be useful to assess the capability of the code to mix fluids. In Fig. 12 we show the density contours (in log-scale) at t = 0.25, 1, 1.75 and 2.5 τ_{KH} using our fiducial SPH scheme. The cloud dissolves within a few τ_{KH} and our results are in qualitative agreement with grid-based methods (Agertz et al. 2007) as well as other improved SPH implementations (Read, Hayfield & Agertz 2010; Read & Hayfield 2012; Hopkins 2013).

4 ISOLATED DISK GALAXY

In this section we present simulations of a more realistic application to a real astrophysical problem: the dynamical evolution of an isolated disk galaxy. These simulations model additional physical processes that are discussed below.

We use the method outlined in Springel, Di Matteo & Hernquist (2005) to set up the initial conditions (see also Moster et al. 2011). The galaxy consists of a stellar and gaseous disk component with a total mass of $3.9 \times 10^{10} \mathrm{M}_\odot$ and a gas fraction of 0.2. The radial scale-length of the


Figure 12. Density distribution (in log-scale) of a central slice at t = 0.25, 1, 1.75, 2.5 τ_{KH} (from top to bottom) for the blob test, using our fiducial SPH scheme ('pe-avsl-ac'). The cloud dissolves within a few τ_{KH} and the results are in qualitative agreement with grid-based methods as well as other improved SPH implementations.

stellar and gaseous exponential profile is 2.5 kpc. The stellar disk has a scale height of 0.6 kpc. The vertical structure of the gaseous disk is determined assuming hydrostatic equilibrium. In addition, the galaxy has a stellar bulge $(9.7 \times 10^9 \mathrm{M}_\odot)$ following a Hernquist (Hernquist 1990) profile with a scale length of 0.3 kpc. The disk galaxy is embedded in a dark matter halo with a virial radius $r_{\mathrm{vir}} = 160$ kpc and a mass $M_{\mathrm{halo}} = 1.3 \times 10^{12} \mathrm{M}_\odot$. The dark matter halo follows also a Hernquist profile with an NFW-equivalent (Navarro, Frenk & White 1997) concentration parameter $c = 9$ such that the scale length $r_s = r_{\mathrm{vir}}/c$. The particle numbers for the different components are $N_{\mathrm{halo}} = 3 \times 10^6$ for the dark matter halo, $N_{\mathrm{disk}} = 3 \times 10^6$ for the stellar disk, $N_{\mathrm{bulge}} = 7.5 \times 10^5$ for the stellar bulge and $N_{\mathrm{gas}} = 6 \times 10^5$ for the gaseous disk. The softening lengths are 68 pc for the dark matter halo and 13 pc for the gas, disk and bulge components. We also set up an initial radial metallicity gradient of -0.04 dex/kpc and $Z = Z_\odot$ at 8 kpc from the galactic center. All details of the model are given in Table 2.

4.1 Cooling and star formation

We adopt the implementation of metal enrichment and cooling presented in Aumer et al. (2013), which is partly based on Scannapieco et al. (2006). We trace 11 individual elements H, He, C, N, O, Ne, Mg, Si, S, Ca and Fe for all gas and star particles. These elements are produced by chemical enrichment of SNII, SNIa and AGB stars and then advected with the particles. For gas particles, we include metal dif-

[3] Available at http://www.astrosim.net/code/doku.php
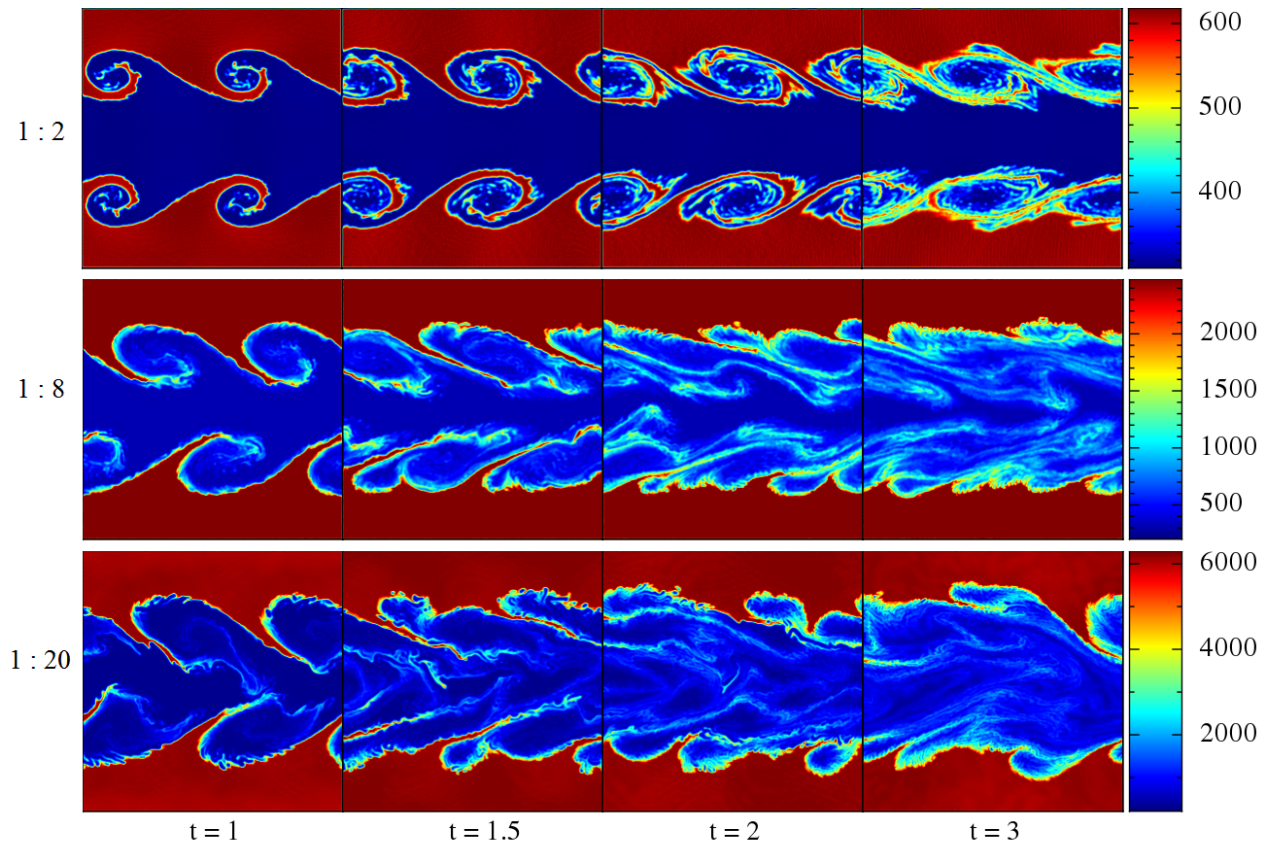
Figure 11. The density distribution (in units of $M_\odot/\mathrm{kpc}^3$) at z = 8 kpc for the KH instability test at t = 1, 1.5, 2, 3 τ_{KH} (from left to right) with a density contrast of 1:2 (top row), 1:8 (middle row), and 1:20 (bottom row). The instability develops in a few characteristic time-scales thanks to the PE formulation.

Table 2. Parameters for the isolated disk galaxy

M_{halo}	1.3×10^{12}	$M_\odot$	halo mass
N_{halo}	3×10^6		halo particle number
v_{cir}	160	km/s	halo circular velocity
c	9		halo concentration
λ	0.035		spin parameter
M_{disk}	3.1×10^{10}	$M_\odot$	stellar disk mass
N_{disk}	3×10^6		disk particle number
r_{disk}	2.5	kpc	disk scale length
h_{disk}	0.6	kpc	disk scale height
M_{gas}	7.8×10^9	$M_\odot$	gas mass
N_{gas}	6×10^5		gas particle number
r_{gas}	2.5	kpc	gas scale length
$d(\log Z)/dr$	-0.04	dex/kpc	metallicity gradient
M_{bulge}	9.7×10^9	$M_\odot$	bulge mass bulge
N_{bulge}	7.5×10^5		bulge particle number
r_{bulge}	0.3	kpc	bulge scale length

fusion (see Aumer et al. 2013 for details) to account for turbulent mixing. The radiative cooling rate of the gas is computed on an element-by-element basis, assuming optically thin gas in ionization equilibrium under the UV/X-ray background as in Wiersma, Schaye & Smith (2009). The minimum temperature is set to 10^2 K.

We adopt a standard estimate for the local star formation rate:

$$\frac{\mathrm{d}\rho_\star}{\mathrm{dt}} = \epsilon \frac{\rho_{\mathrm{gas}}}{\mathrm{t}_{\mathrm{dyn}}}, \tag{30}$$

where $\mathrm{t}_{\mathrm{dyn}}$ is the local dynamical time $(4\pi G\rho_{\mathrm{gas}})^{-0.5}$, ϵ is the star formation efficiency, $\rho_\star$ and ρ_{gas} are the volumetric density of stellar and gas component respectively. We take $\epsilon = 0.04$ as our default choice. The star formation threshold is set to a number density of $n_{\mathrm{gas}}^{\mathrm{th}} \geqslant 1$ cm^{-3} and we require the temperature to be $T \leqslant 10^4$ K. Gas particles that are either too hot or too dilute will not participate in the star formation process.

For the stellar feedback we only consider mass, momentum and energy input from SN explosions. We assume that the SN events (about ~ 3 Myr after a stellar particle has formed) transfer mass, radial momentum, and thermal energy to the nearest 10 gas particles in a free-expansion approximation (Ostriker & McKee 1988). The mass of the supernova ejecta (typically ~ 19 per cent of the formed stellar population) is directly added to its neighbors and distributed in a kernel-weighted fashion. Each individual supernova explosion injects 10^{51} ergs into the ISM, which corresponds to an ejecta velocity $v_e \sim 3000$ km/s. The momen-

tum is transferred to the neighbors similar to an inelastic collision and the "post-shock" gas velocity is

$$\mathbf{v}'_{\mathrm{gas}} = \frac{m_{\mathrm{gas}}\mathbf{v}_{\mathrm{gas}} + \Delta m \mathbf{v}_e}{m_{\mathrm{gas}} + \Delta m}. \tag{31}$$

The remaining energy is transformed into thermal energy and added to the affected gas particles

$$\Delta U = \frac{1}{2}\frac{m_{\mathrm{gas}}\Delta m}{m_{\mathrm{gas}} + \Delta m}|\mathbf{v}_e - \mathbf{v}_{\mathrm{gas}}|^2. \tag{32}$$

This feedback implementation conserves mass, momentum and energy simultaneously. The injected momentum is small (as we do not assume a Sedov approximation) but it will not be radiated away easily, so the feedback can be more efficient, especially in the dense clumps of gas. As we will show below this feedback implementation naturally drives outflows from the galactic disk.

4.2 Evolution of the gaseous disk

It has been shown that the method for setting up initial conditions presented in Springel, Di Matteo & Hernquist (2005) produce stable models for disk galaxies, also in the presence of gas (see e.g. Moster et al. 2010, 2012). We refer to these papers for all necessary details. In this section we only focus on the impact of a specific SPH implementation on the gas phase properties while keeping the star formation algorithm fixed. For this comparison we model the dynamical evolution for ~ 1 Gyr and investigate the morphology of the gas disk and the rates of star formation, outflow from the disk.

As mentioned in Section 2.3, we adopt a 'strong limiter' in our fiducial AV scheme as opposed to a 'weak limiter' first explored by Cullen & Dehnen (2010). The motivation is that the AV scheme with a weak limiter seems to be too viscous in our isolated disk simulations. In this section we study the impact of these two different limiters on the evolution of the gaseous disk, particularly the distribution of the gas density.

4.2.1 Density-entropy formulation

In Fig. 13 we show the evolution of the gas density (face-on) using the density-entropy (DE) formulation of SPH with different dissipation schemes. The standard constant viscosity with a Balsara switch is shown in the top row. We find that some small "holes" form in the central part of the disk and gradually grow to kpc size and then start to be sheared away. They seem to be related to the stellar feedback as the SN explosions create bubbles in the surrounding ISM (though on a much smaller scale). However, similar holes also form at large radii, where star formation is unimportant. The question is whether the formation and growth of these bubbles through merging is physical and whether it is caused by feedback or is an artifact of too much viscosity due to the numerical implementation, similar to the Keplerian ring (see Section 3.5). We therefore test the AV switch with a weak limiter, which does not lead to instabilities in the Keplerian ring. However, the situation becomes even more problematic on a shorter time scale (second row of Fig. 13). After 600 Myrs almost the entire gas is evacuated from the disk which is clearly too severe to be realistic. The situation is improved if we include AC (third row). However, it only delays the instability for a few Myrs.

With our fiducial AV with a strong limiter these holes disappear both without AC (fourth row) as well as with AC (bottom row). If we include the AC the disk becomes smoother and clear spiral arms are formed. As discussed in Section 2.3 the main feature of the 'strong limiter' implementation is that the viscosity coefficient is always smaller than the limiter ξ_i (times the constant maximum value $\alpha_{\max}$ which we set to be 1).

We interpret the evolution of the 'avwl' models as a viscous instability, eventually triggered by SN-induced blast waves. In Fig. 14 we show the histograms of the viscosity coefficients for all gas particles in the weak and strong limiter case. In case of the weak limiter the disk is clearly much more viscous. The viscosity coefficient is above the minimum value of 0.1 for almost all particles and peaks at around $\alpha_i = 0.8$. With a strong limiter the majority of the particles retain their minimum value $\alpha_i = 0.1$. We therefore interpret the instability as a result of having too much viscosity. The physical explanation is the following: in the low viscosity (strong limiter) case, the small holes created by the SN explosions are quickly sheared away before they have the chance to merge. On the other hand, if the viscosity is generally too high or decays too slowly in the post-shock regions, the holes become too viscous to be sheared away by the differential rotation. As such, they merge and trigger even more shocks, leading to the catastrophic instability. The strong limiter efficiently suppresses viscosity in the rotating disk and thus avoids such instability.

4.2.2 Pressure-entropy formulation

We perform the same set of simulations as in Section 4.2.1 but now with the PE formulation. Fig. 15 shows the results at t = 500, 700, and 900 Myr. The onset of the instability is significantly delayed with the PE formulation in all cases. With a weak AV limiter, the disk remains stable for a much longer time (until t = 500 Myr) than for the DE case. However, it still becomes unstable if we run the simulations up to 1 Gyr. For constant viscosity (plus Balsara switch, top row of Fig. 15) as well as the AV switch with a strong limiter (two bottom rows of Fig. 15), the disk remains stable at all times and distinct spiral arms are formed. Fig. 16 shows the corresponding histogram of the viscosity coefficient for different AV schemes which looks very similar to the DE implementation (Fig. 13). This suggests that the artificial surface tension in the DE formulation also plays a role for the onset and evolution of the instability. In the DE formulation, the boundaries between hot and dilute post-shock bubbles and its surrounding cold and dense ISM are difficult to break once being created.

We tentatively conclude that the instability is a consequence of having too much viscosity in the disk, supported by spurious surface tension. Including AC or using the PE-formulation both alleviate the situation. However, the best "solution" is to avoid too much viscosity in the first place. On the other hand, having too little viscosity is also dangerous as it is required for proper shock modeling. The key is therefore to introduce an appropriate amount of viscosity in the "right" places. Our AV scheme (with a strong limiter) delivered reassuring results for the Sedov explosion test. However, in galactic disks where both shocks and shear flows coexist, it is unclear how much viscosity should be in-
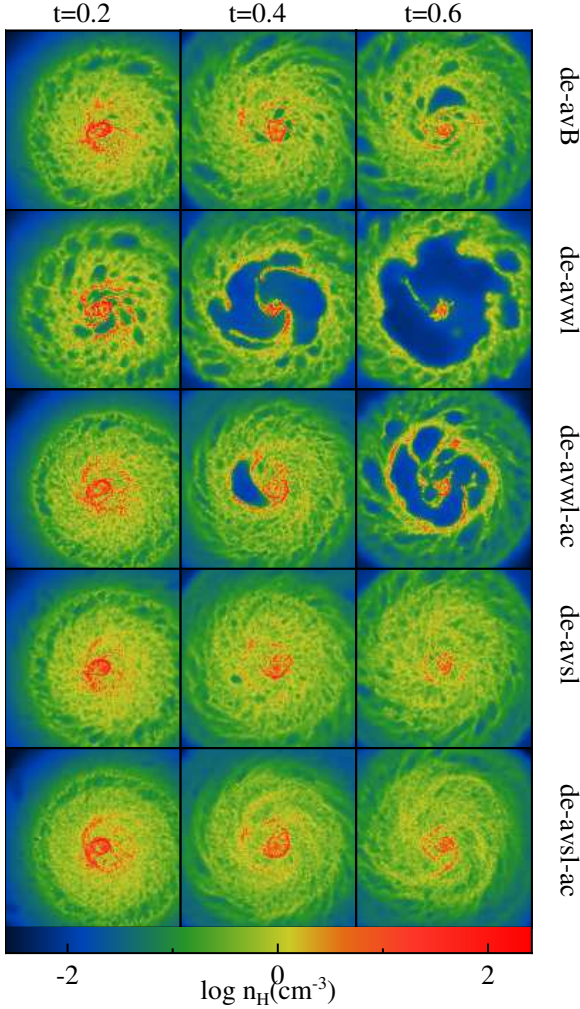
Figure 13. The projected density of gas (face-on) in the isolated disk simulation with different SPH schemes (from top to bottom) at t = 200 (left column), 400 (middle column), and 600 (right column) Myrs respectively. The SPH schemes all use the DE formulation but with different dissipation schemes. *Top row:* Constant AV with a Balsara switch creates holes that gradually merge but are sheared away. *Second row:* With weak AV limiter the holes merge and the instability evacuates most of the gas in the disk. Including AC mitigates the situation (third row). *Two bottom rows:* The AV switch with a strong limiter makes the disk gas less viscous and the instability does not develop, both with and without AC .

troduced. This is a general issue for most SPH schemes that rely on AV for shock capturing. An exception might be 'Godunov SPH' (e.g. Cha, Inutsuka & Nayakshin 2010, Murante et al. 2011) which does not rely on artificial viscosity for shock capturing.

4.3 Thermaldynamic properties

We show in Fig. 17 the phase diagrams of four different SPH schemes ('de-avsl', 'de-avsl-ac', 'pe-avsl', and 'pe-avsl-ac') at t = 300 Myr. The majority of the gas follows a locus of thermal equilibrium where the cooling balances heating. The SN feedback injects both thermal energy to the gas which raises
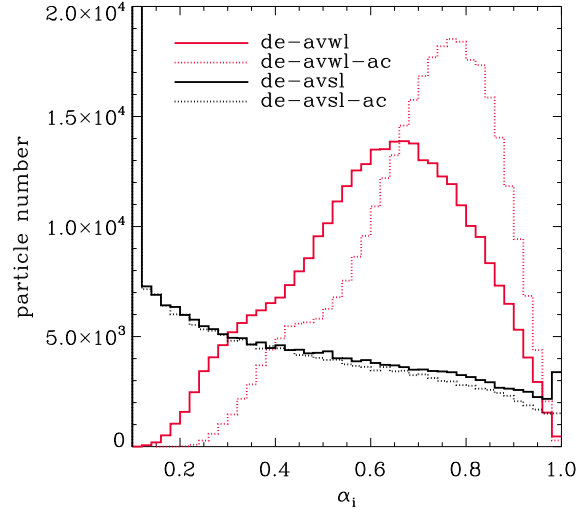
Figure 14. Histogram of the AV coefficient in the isolated disk simulation at t = 300 Myr using the DE-formulation. The AV coefficient with a weak limiter (red solid and dotted lines) peaks at 0.6-0.8, while with a strong limiter (black solid and dotted lines) most particles retain the minimum value $\alpha_i = 0.1$.

the temperature to $\gtrsim 10^6$ **K at density $\sim$ 1 cm^{-3} as well as kinetic energy which helps to dissolve the dense clumps. The highly over-pressurized hot gas drives the ambient ISM into galactic outflows. Once the gas is pushed out of the disk, radiative cooling and heating becomes inefficient due to the low density, and the temperature and density of the gas follows an adiabatic relation $T \propto \rho^{\gamma-1}$ (dashed lines). Fluid mixing provides an extra channel for the hot gas to cool. Therefore, a fraction of hot gas drops rapidly to low temperatures. Indeed, for the models that includes AC (right panels), we see more gas around $\rho \sim$ 10 cm^{-3} and $T \sim 10^{3.5}$ K, as a result of more efficient mixing. There is also a small amount of gas at $\rho \sim$ 10 cm^{-3} and $T \sim 10^{4.5}$ K in all cases, which is due to the local minimum of the cooling curve at that temperature. More quantitatively, the phase diagram can be divided into different phases by defining the cold (hot) disk gas as $T \leqslant 10^5$ K $(T > 10^5$ K) and $|z| <$ 5kpc, and the outflow/inflow gas as $|z| \geqslant$ 5kpc, where z = 0 is the disk plane. From panel (a) to (d) in Fig. 17, the mass fraction of the hot disk gas is $0.54\%, 0.22\%, 0.34\%$ and 0.17%, while the mass fraction of the outflow/inflow gas is $5.16\%, 1.25\%, 1.3\%$ and 0.61%, respectively (the rest is the cold disk gas). In our fiducial model (panel d) where mixing is the most efficient, the mass fraction of cold (hot) disk gas is the largest (smallest), while the amount of outflow is almost an order of magnitude smaller than the 'de-avsl' model. Since the hot gas in the disk cools faster due to more efficient fluid mixing, the effect of feedback is weakened and the amount of outflow decreases. We will discuss the outflow in more detail in the next section.**
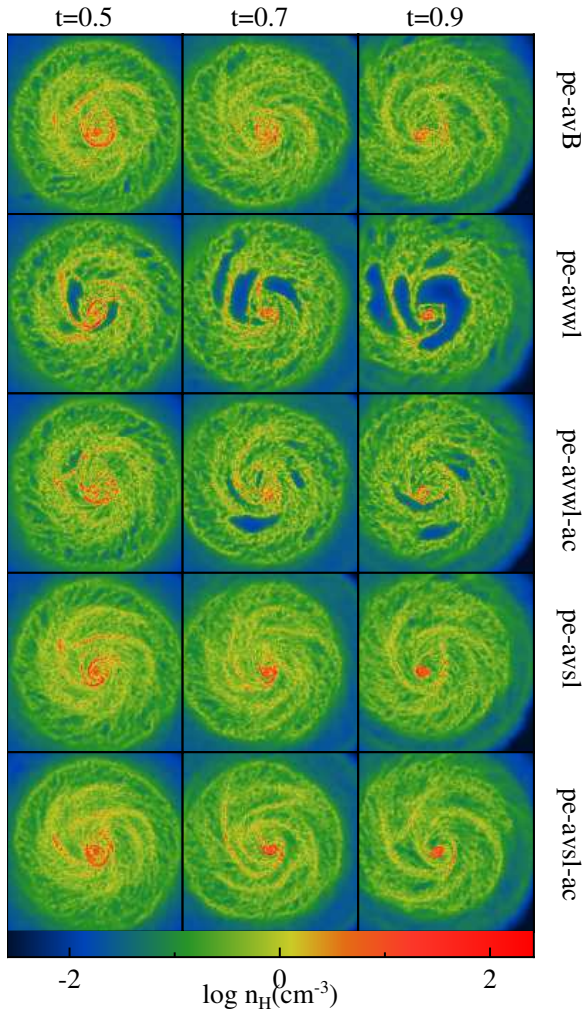
Figure 15. Same as Fig. 13 but for the PE SPH scheme at t = 500 (left column), 700 (middle column), and 900 (right column) Myrs. The PE formulation significantly alleviates the instability. However, large holes still form using a weak limiter, as a result of the disk gas being too viscous.

4.4 Star formation and galactic outflows

In this section we investigate the global star formation rate (SFR) as well as the outflow rate from the galactic disk for the different SPH schemes. We show in Fig. 18, panel (a), the time evolution of SFR. Surprisingly, there is no obvious difference in terms of SFR between the traditional constant AV and our variable AV, despite the presence of the instability in the former. This is because the SFR is mainly determined by the total amount of the star forming gas and is not too sensitive to the morphology of the gas. Including AC or using the PE formulation both increase the overall SFR by about a factor of two. This is a consequence of more efficient mixing between the hot and cold gas, which leads to the presence of more cold gas available for star formation, in agreement with Hopkins (2013). The gradually declining SFR is expected as the total amount of star-forming gas is continuously depleted either by galactic outflows or the star formation itself.

Fig. 18, panel (b), shows the mass loading η, defined as the ratio of the outflow rate to the SFR. The outflow rate is
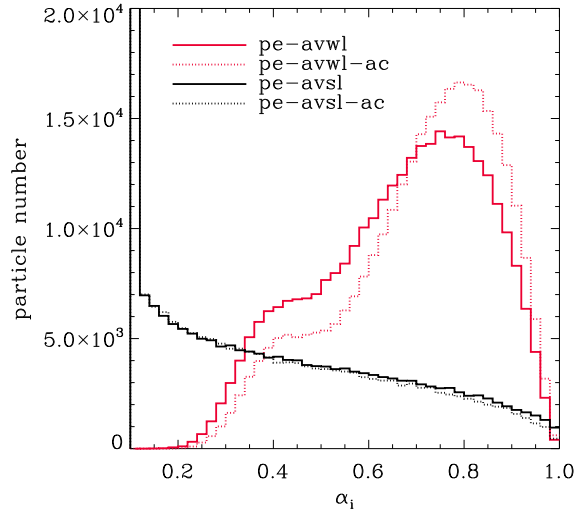
Figure 16. Same as Fig. 14 but using the PE scheme with no obvious differences from the DE scheme.

computed by summing the total mass of gas particles passing through a plane at z = ± 5 kpc, where the z-axis is the rotation axis of the disk. There is an initial burst of outflow in all cases caused by the initial setup. Since all the gas particles are initially located in the disk, the environment outside of the disk is a vacuum which allows an unimpeded outflow triggered by the SN explosions. These outflowing particles will be pulled back down to the potential well of the disk due to gravity, leading to the onset of gas inflow which can interact with the subsequent outflow. Eventually the inflow and outflow reach a quasi-steady state and a hot gaseous halo is formed (after ∼ 150 Myrs). A small fraction of the gas can even escape the halo completely. The mass loading η shows a strong dependence on the adopted SPH schemes: both the PE formulation and the AC suppress the mass loading. One direct explanation is that the increased SFR transforms part of the gas into stars, thus reducing the amount of gas available to the outflow. However, the mass loading drops almost an order of magnitude between the two most extreme cases while the difference of SFR is only about a factor of 2. This suggests that the feedback efficiency is directly affected by the SPH implementation. As it becomes weaker (for AC and PE models) the hot gas cannot be blown out of the disk as efficiently. The driving force of the shock is dissipated as the shocked heated particles are continuously mixed with the ambient cold ISM. We also observe that the effect (reduced mass loading) seems stronger at higher resolution due to more efficient mixing. This is contrary to Hopkins et al. (2013) where they find both the SFR and mass loading are insensitive to the adopted SPH scheme. The discrepancy might be due to the different feedback implementation: in Hopkins et al. (2013) the contribution of momentum input (the radiation pressure) is significant, which is expected to be less affected by fluid mixing.

We further investigate the star formation rate and the mass loading using a different initial condition which may
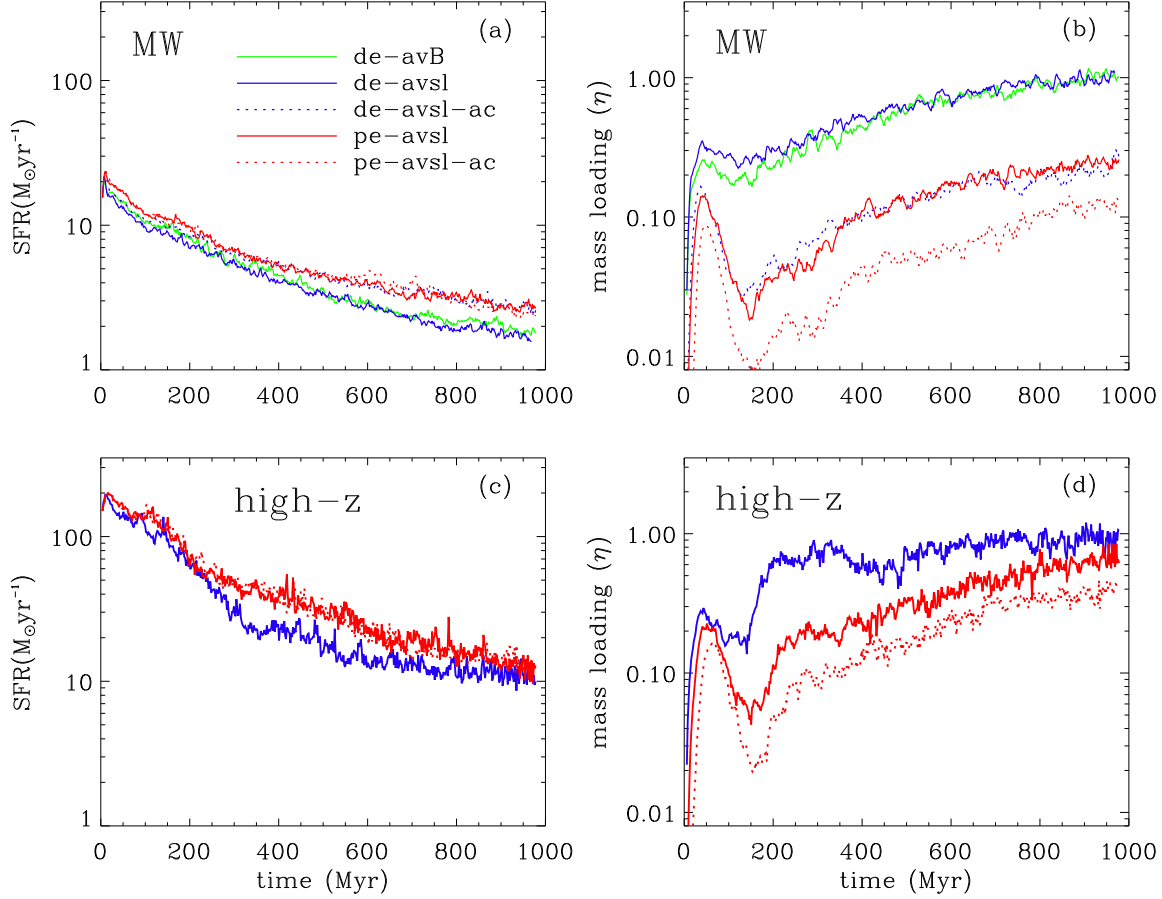
Figure 18. The star formation rate and mass loading as a function of time for a Milky-Way like galaxy (panel (a), (b)) and a high-redshift galaxy (panel (c), (d)), using different SPH schemes: DE using constant viscosity plus the Balsara switch (de-avB, green line), DE using variable strong limiter AV without (de-avsl, blue line) and with (de-avsl-ac, blue dashed line) artificial conduction, and PE using a variable AV without (pe-avsl, red line) and with (pe-avsl-ac, red dashed line) AC. While the SFR shows only a weak dependence on the adopted SPH scheme, the outflow rate (hence the mass loading) is much more sensitive to the adopted SPH scheme.

represent a gas-rich high-redshift disk galaxy, set up by the same method as in Section 4. The galaxy contains $6.4 \times 10^{10} M_\odot$ of gas and $2.7 \times 10^{10} M_\odot$ of stars in the disk, and a stellar bulge of $6.4 \times 10^{10} M_\odot$. The dark matter halo follows a Hernquist profile with a concentration of 3.5 and a mass of $1.5 \times 10^{12} M_\odot$. Again we set a radial metallicity gradient of -0.04 dex/kpc. The particle numbers for the different components are $N_{\rm halo} = 3 \times 10^5$ for the dark matter halo, $N_{\rm disk} = 3 \times 10^5$ for the stellar disk, $N_{\rm bulge} = 7 \times 10^5$ for the stellar bulge and $N_{\rm gas} = 7 \times 10^5$ for the gaseous disk. The softening lengths are 100 pc for the dark matter halo and 20 pc for the gas, disk and bulge components. Half of the gas follows an exponential profile with a scale length of 3 kpc, while the other forms an extended flat disk with a radius of 15 kpc. The scale height of the stellar disk is 0.3 kpc and the scale length of the bulge is 1.2 kpc. Fig. 18, panel (c), shows the star formation rate with three different SPH schemes: 'de-avsl', 'pe-avsl', and 'pe-avsl-ac'. As in the Milky Way case, the SFR differs only slightly for different SPH schemes, though a systematic increase can still

be seen for schemes that promote mixing. Interestingly, the mass loading in Fig. 18, panel (d), becomes less sensitive to the adopted SPH scheme compared to the Milky Way case, which is in better agreement with Hopkins et al. (2013). The difference between the two extreme cases is only a factor of two after the quasi-steady state has reached (~ 400 Myr). One possible explanation is that the star formation rate is so high so that it drives outflow more easily despite the increased capability of fluid mixing. From the test cases presented here - and for this specific feedback implementation - it seems that with the traditional SPH ('de-avsl') the outflow properties (mass loading of order unity) are independent of the initial conditions (star formation rate). On the other hand, our fiducial model ('pe-avsl-ac') has a factor of 10 lower mas loading for the MW disk and only a factor of ~ 3 lower mass-loading for the high-z disk. Apparently this introduces a SFR dependent mass-loading. **The outflow velocity also depends on the adopted SPH scheme. The mean velocities projected on z-axis at $z = \pm 5$ kpc, after reaching a quasi-steady state,**
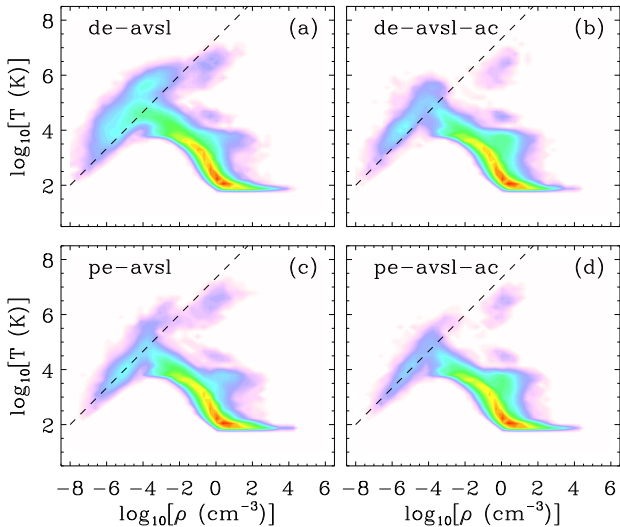
Figure 17. The phase diagram of four different SPH schemes at t = 300 Myr. *Panel (a):* DE formulation without AC. *Panel (b):* DE formulation with AC. *Panel (c):* PE formulation without AC. *Panel (d):* PE formulation with AC. The dashed line is the adiabatic relation $T \propto \rho^{\gamma-1}$. The majority of the gas is cold ($< 10^4$ K) and follows a locus of thermal equilibrium where cooling balances heating. The SN-induced hot gas ($\gtrsim 10^6$ K) on the disk is driving galactic outflows. Outflowing gas, once being pushed out of the disk, has a long cooling time due to its low density and therefore follows an adiabatic relation. Hot gas cools faster with more efficient fluid mixing and therefore the amount of outflow decreases.

are about 200, 140, and 100 km/s for the 'de-avsl', 'pe-avsl', and 'pe-avsl-ac' model, respectively. This trend is consistent with the picture that fluid mixing suppresses outflows. We refrain from a detailed comparison with observations as the main goal of this work is to investigate the effect of different SPH schemes.

4.5 Accretion from the hot gaseous halo

In this section we investigate the properties of hot halo gas that might be accreting onto the disk. A hot gaseous halo is added to the Milky-Way like disk using the method presented in Moster et al. (2011). The density follows a β-profile:

$$\rho_{\rm hg}(r) = \rho_0 \left[1 + \left(\frac{r}{r_{\rm c}} \right)^2 \right]^{-1.5\beta}, \qquad (33)$$

where ρ_0 is the core density, r_c is the core radius and β describes the slope of the profile at large radii. We set $r_c = 0.22 r_s$ and $\beta = 2/3$ as in Moster et al. (2011). The core density ρ_c is determined by the total baryonic fraction f_b within the virial radius $r_{\rm vir}$. We set $f_b = 0.12$ such that the mass of the hot gaseous halo within $r_{\rm vir}$ is $M_{\rm hg} = 6.54 \times 10^{10} {\rm M}_\odot$. The temperature profile is determined assuming hydrostatic equilibrium at a given radius. The hot gaseous halo is rotating along the rotation axis of the disk where the specific angular momentum of the gas is α-times the the specific angular momentum of the dark matter halo. We set

$\alpha = 4$ following Moster et al. (2011) who found this choice to agree best with observational constraints. The metallicity of the hot gaseous halo is set $Z = 0.3\, Z_\odot$ based on observations of Milky Way's hot gaseous halo (Miller & Bregman 2013). The particle numbers for different components are $N_{\rm halo} = 6 \times 10^5$ for dark matter halo, $N_{\rm disk} = 4.8 \times 10^5$ for the stellar disk, $N_{\rm bulge} = 1.5 \times 10^5$ for the stellar bulge, $N_{\rm cg} = 1.2 \times 10^5$ for the cold gaseous disk, and $N_{\rm hg} \approx 1.3 \times 10^6$ for the hot gaseous halo. The individual particle mass is five times larger than in Section 4.2 and 4.4. The softening lengths are 100 pc for the dark matter halo and 20 pc for the gas, disk and bulge components.

Fig. 19 shows the gas density at t = 1.8 Gyr using different SPH schemes in both face-on and edge-one views. The morphological difference in accretion properties is striking: in the 'de-avsl' case, the inflowing gas forms small blobs which are purely numerical artifacts due to the lack of proper fluid mixing. Including AC efficiently eliminates these blobs, which is in agreement with Hobbs et al. (2013). The PE formulation ('pe-avsl') also prevents such blobs, while the accretion morphology is different from the 'de-avsl-ac' case; the latter is smoother and more filamentary. This might reflect the difference of mixing mechanisms between AC and PE formulation. The PE formulation allows mixing only in a dissipation-less way; mixing occurs via turbulent motion with entropy still conserved at particle level. On the other hand, AC explicitly smooths the entropy gradient and therefore the morphology is expected to be smoother. Our fiducial model combines both ('pe-avsl-ac') and shows also filamentary structures. **Hobbs et al. (2013) found that in their favored SPH scheme (SPHS) which avoids numerical blobs by AC, the accreting overdense filaments are able to fragment into clumps via nonlinear thermal instability triggered by the SN-driven outflows. We do not find such fragmentation in out fiducial model probably because our feedback is too weak to induce enough nonlinear over-densities.**

5 SUMMARY & DISCUSSION

In this paper we study the performance of different algorithmic implementations of the SPH code GADGET for a variety of idealialized hydrodynamic tests including the Gresho, Sod shock tube, Sedov explosion, 'equilibrium square', Keplerian ring, Kelvin-Helmholtz, and the 'blob' test (Section 3). We also test the impact on the dynamical evolution of a Milky Way like disk galaxy - including cooling from a hot gaseous halo - as well as a gas-rich high-redshift disk galaxy including metal cooling, metal enrichment, star formation and feedback from supernova explosions.

We test a density-entropy and a pressure-entropy formulation in combination with recently proposed implementations for the treatment of artificial viscosity and conduction (Section 2). The study indicates that implementations with a pressure-entropy formulation (Saitoh & Makino 2013; Hopkins 2013) in combination with a Wendland C^4 kernel with 200 neighbors, variable artificial viscosity with higher order shock detection (Cullen & Dehnen 2010) and artificial conduction (Price 2008; Read & Hayfield 2012) pass all idealized hydrodynamic tests.
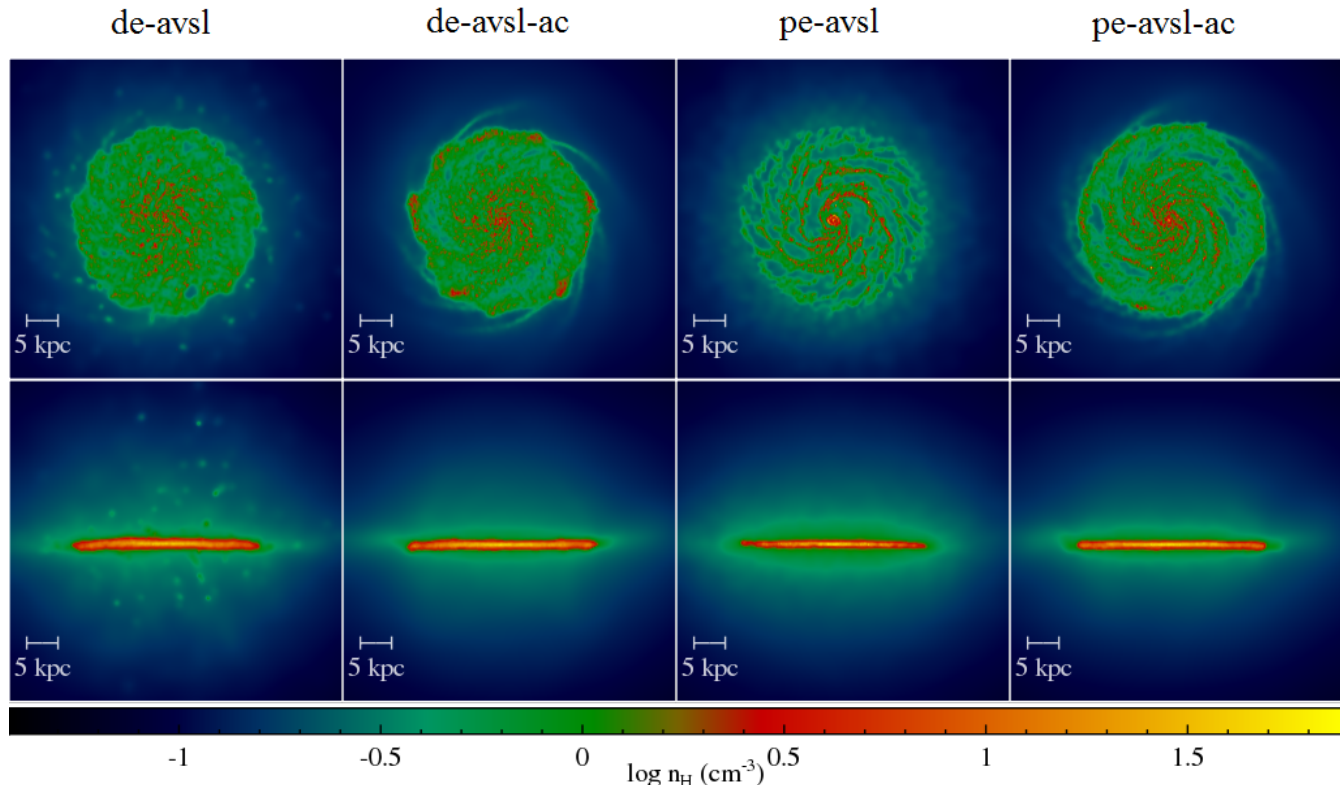
Figure 19. The face-on (top row) and edge-on (bottom row) views of the projected gas density at $t = 1.8$ Gyr, with four different SPH schemes. *First column*: DE formulation without AC (de-avsl). *Second column*: DE formulation with AC (de-avsl-ac). *Third column*: PE formulation without AC (pe-avsl). *Fourth column*: PE formulation with AC (pe-avsl-ac). The 'de-avsl' scheme leads to blobs which are purely numerical artifacts due to the lack of proper fluid mixing. These problematic blobs can be efficiently avoided by either including AC or PE formulation (or both).

We propose a modified implementation for artificial viscosity with a strong viscosity coefficient limiter with high sensitivity to the velocity curl (Section 2.3). In addition to passing all the idealized tests, our fiducial implementation performs very well for the disk evolution simulations, where some other implementations can develop a viscous instability (Section 4). Despite the successes our fiducial code still shows weaknesses in low Mach number shear flows and the rate of convergence. Still, the above results indicate improvements with respect to most standard SPH implementations (e.g. Springel 2005; Wetzstein et al. 2009; Hubber et al. 2011). **These improvements, along with the advantages discussed in the introduction, keep SPH a competitive numerical method. Comparison between results of SPH and grid-based methods (e.g. Teyssier 2002; Bryan et al. 2014) can also provide important information as they have very different numerical artifacts and are highly complementary.**

The actual algorithmic implementation has a significant impact on the gas outflow properties of our disk evolution models. Implementations with better fluid mixing capabilities in general result in reduced mass loading. In the Milky Way case, our fiducial implementation has about an order of magnitude lower mass loading compared to a standard implementation, while at the same time the star formation rate is only slightly higher. For the gas-rich, high-redshift

disk model, the mass loading becomes less sensitive (but still notable) to the adopted SPH scheme. In addition, we demonstrate that either artificial conduction or a pressure-entropy formulation (or both) suppresses the formation of artificial cold blobs. **We note that the star formation model as well as the feedback recipe have also significant impact on the evolution of galaxies (e.g., Sales et al. 2010, Scannapieco et al. 2012). However, an accurate scheme for the hydrodynamics is equally (if not more) important, as the star formation and feedback models need to be calibrated under the 'correct' hydrodynamics. The impact of star formation and feedback models will be addressed in future work.**

In Table 3, we present a summary of all tests in this paper. SPH implementations marked with '✓' passed the respective test while those marked with '×' failed. Again, these tests indicate that SPH can perform well with a more accurate kernel, a pressure-entropy formulation, artificial viscosity with a strong, curl sensitive limiter and a higher order shock indicator and artificial conduction. Our fiducial implementation, which we term SPHGal, passes all tests. [4]

---

[4] We find (not shown) that the weak limiter scheme 'pe-avwl-ac' also passes all of the idealized tests that might show differences with the strong limiter (i.e. shock tube, Sedov, Keplerian ring

Table 3. Summary of the results of the idealized hydrodynamic tests in Section 3 and the galactic disk test in Section 4. SPH implementations marked with ✓ passed the test while those marked with × failed the test. Our fiducial implementation 'pe-avsl-ac' passed all tests.

Test	SPH scheme	Results
Gresho	de-avB (cs64)	×
	de-avsl-ac (wld200)	✓
	pe-avsl-ac (wld200)	✓
Shock tube	pe-avsl-ac	✓
	pe-avwl-ac	✓
Sedov	de-avsl	✓
	pe-avsl	×
	de-avsl-ac	✓
	pe-avsl-ac	✓
	pe-avwl-ac	✓
	pe-avsl-ac-erho	×
Keplerian ring	de-avB-lvg	×
	pe-avsl-ac-lvg	×
	de-avB	×
	pe-avsl-ac	✓
	pe-avwl-ac	✓
Hydrostatic	de-avsl-ac	×
	pe-avsl	✓
	pe-avsl-ac	✓
Kelvin-Helmholtz	pe-avsl-ac	✓
Blob	pe-avsl-ac	✓
	pe-avwl-ac	✓
Galactic disk	de-avB	×
	de-avwl	×
	de-avwl-ac	×
	de-avsl	✓
	de-avsl-ac	✓
	pe-avB	✓
	pe-avwl	×
	pe-avwl-ac	×
	pe-avsl	✓
	pe-avsl-ac	✓

In the follwing we discuss our main results in more detail:

• With the PE formulation the spurious surface tension at contact discontinuities is eliminated by construction and fluid mixing can be modeled properly without the help of AC (Read, Hayfield & Agertz 2010; Saitoh & Makino 2013; Hopkins 2013). We therefore suppress AC in shear flows to prevent over-mixing by including a quadratic limiter similar to the Balsara switch (Section 2.4). Another advantage of this limiter is that it avoids unwanted conduction in a self-gravitating system in hydrostatic equilibrium.

• It is necessary to include the AC in the PE formulation if strong shocks are involved (Section 3.4). The weakness of the PE formulation stems from the entropy-weighted sum in the pressure estimate, which makes the results noisy and

and the blob test). It only fails in the disk simulation, where both shocks and shear flows coexist.

even biased if the entropy variation is large from one particle to another. Including AC greatly improves the results in the Sedov explosion test. In addition, the entropy-weighted density gives a biased estimate (the pre-shock 'bump') in the Sedov explosion test even when the particles are distributed regularly. The mass-weighted density is a more reliable estimate and should be used whenever the information of density is needed. Indeed, the only entropy-weighted quantity we use is the pressure estimate in the equation of motion. Using the entropy-weighted density in the dissipation terms leads to an incorrect prediction of the shock position.

• We find a feedback-driven instability developing in a typical isolated disk galaxy if the gaseous disk becomes too viscous. The hot bubbles created by SN explosions are too viscous to be sheared away by the differential rotation. They merge with one another and eventually form large holes in the disk. The AV switch with a strong limiter is able to suppress the viscosity so that the disk remains stable. On the other hand, it could also be possible that it suppresses viscosity too much and cannot capture shocks properly. However, the Sedov explosion test is recovered equally well and provides credibility for our modified AV scheme. In the cases where both shocks and shear flows coexist, it is in fact difficult to determine how much viscosity is appropriate. Compromises have to be made between properly modeling shocks and avoiding artificial shear viscosity. This seems to be a general issue for most SPH schemes that use AV for shock capturing (an exception might be 'Godunov SPH', e.g. Cha, Inutsuka & Nayakshin 2010, Murante et al. 2011). Adopting the PE formulation and including AC alleviates the situation, which suggests that spurious surface tension also plays a role for the instability. The boundaries between the hot bubbles and the cold ISM are sustained by the spurious surface tension in the DE formulation. As such, they are difficult to destroy once being created.

• We have investigated the star formation rate as well as the mass loading of the disk galaxy models with different SPH schemes. The SFR increases slightly when we adopt the SPH schemes that allow more efficient fluid mixing. Here the hot gas in the disk (created by SN explosions) is continuously mixed with the large amount of cold gas and therefore cools faster. For this reason, the amount of cold gas available to star formation is higher. The mass loading is affected even more and drops by almost an order of magnitude (in the MW case) from a standard SPH implementation to our fiducial implementation. This is partly related to the increased SFR that transforms some of the gas into stars. In addition, the continuous mixing with the ambient ISM weakens the driving force of the shock-heated particles and hence decreases the mass loading. This is in contrast to Hopkins et al. (2013) who have made similar improvements to their SPH scheme and claim that they in general find little difference in SFR as well as the mass loading using different SPH schemes. **The discrepancy may arise from the different feedback models. It is expected that the thermal feedback would be more sensitive to the fluid mixing, as mixing provides an extra channel for the hot gas to cool and thus weakens the feedback. However, we note that the kinetic feedback would still convert some fraction of kinetic energy into thermal energy via shock heating and therefore is not completely unaffetced by mixing.** In the case of the gas-rich, high-

redshift disk model, the mass loading becomes less sensitive to the adopted SPH scheme, which is in better agreement with Hopkins et al. (2013). One possible explanation is that the higher star formation rate drives the outflow more efficiently despite the increased capability of fluid mixing and hence weakening the differences.

• We investigate the accretion behavior of the hot gas halo onto the Milky Way like disk. As commonly being criticized in the literature, the traditional SPH (DE without conduction) generates plenty of small blobs due to the lack of proper fluid mixing. Including AC efficiently eliminates these blobs, in agreement with Hobbs et al. (2013). The PE formulation, with or without AC, is also capable of eliminating the blobs. In addition, depending on the presence of AC, the accretion morphology shows notable difference: inflowing gas forms smooth filamentary structures if AC is included. This might originate from the different mixing mechanism between AC and PE formulation. In PE formulation, mixing is a dissipation-less, entropy-conserving process that relies on turbulent motion. Hot and cold gas do not mix if the turbulent motion is weak. On the other hand, AC promotes mixing by explicitly smoothing out entropy differences, leading to smoother morphology.

In summary, we have presented an updated SPH implementation SPHGal that performs more accurately in several idealized hydrodynamic tests. The outstanding problem in the traditional SPH, i.e. the poor capability of fluid mixing, no longer exists thanks to the PE formulation. In addition, we have a controllable diffusion mechanism (the artificial conduction) similar to the implicit numerical diffusion in the grid-based methods. The higher order velocity gradients prevent false triggering of AV. The AV switch, which involves a strong limiter, is able to capture shocks properly and also to avoid too much viscosity in a disk galaxy. The convergence rate is significantly improved (still slower than the grid-based methods) and shows no sign of saturation with increasing resolution, though the intrinsic issue remains when we move further into the subsonic regimes. We conclude that, with all the modifications, SPHGal is an accurate and valuable numerical method for galaxy formation simulations and many other astrophysical applications.

References

Agertz O. et al., 2007, MNRAS, 380, 963

Aumer M., White S. D. M., Naab T., Scannapieco C., 2013, MNRAS, 434, 3142

Balsara D. S., 1989, PhD thesis, Univ. Illinois at Urbana-Champaign

Balsara D. S., 1995, Journal of Computational Physics, 121, 357

Bauer A., Springel V., 2012, MNRAS, 423, 2558

Brookshaw L., 1985, Proceedings of the Astronomical Society of Australia, 6, 207

Bryan G. L. et al., 2014, ApJS, 211, 19

Cartwright A., Stamatellos D., Whitworth A. P., 2009, MNRAS, 395, 2373

Cha S.-H., Inutsuka S.-I., Nayakshin S., 2010, MNRAS, 403, 1165

Cullen L., Dehnen W., 2010, MNRAS, 408, 669

Dehnen W., Aly H., 2012, MNRAS, 425, 1068

Dolag K., Vazza F., Brunetti G., Tormen G., 2005, MNRAS, 364, 753

Durier F., Dalla Vecchia C., 2012, MNRAS, 419, 465

Feng Y., Di Matteo T., Croft R., Khandai N., 2013, ArXiv e-prints

Gingold R. A., Monaghan J. J., 1977, MNRAS, 181, 375

Gresho P. M., Chan S. T., 1990, International Journal for Numerical Methods in Fluids, 11, 621

Heitsch F., Naab T., Walch S., 2011, MNRAS, 415, 271

Hernquist L., 1990, ApJ, 356, 359

Hobbs A., Read J., Power C., Cole D., 2013, MNRAS, 434, 1849

Hopkins P. F., 2013, MNRAS, 428, 2840

Hopkins P. F., Keres D., Onorbe J., Faucher-Giguere C.-A., Quataert E., Murray N., Bullock J. S., 2013, ArXiv e-prints

Hubber D. A., Batty C. P., McLeod A., Whitworth A. P., 2011, A&A, 529, A27

Hubber D. A., Falle S. A. E. G., Goodwin S. P., 2013, MNRAS, 432, 711

Junk V., Walch S., Heitsch F., Burkert A., Wetzstein M., Schartmann M., Price D., 2010, MNRAS, 407, 1933

Kawata D., Okamoto T., Gibson B. K., Barnes D. J., Cen R., 2013, MNRAS, 428, 1968

Lucy L. B., 1977, AJ, 82, 1013

Miczek F., 2013, PhD thesis, Technische Universitt Mnchen

Miller M. J., Bregman J. N., 2013, ApJ, 770, 118

Monaghan J. J., 1997, Journal of Computational Physics, 136, 298

Morris J. P., Monaghan J. J., 1997, Journal of Computational Physics, 136, 41

Moster B. P., Macciò A. V., Somerville R. S., Johansson P. H., Naab T., 2010, MNRAS, 403, 1009

Moster B. P., Macciò A. V., Somerville R. S., Naab T., Cox T. J., 2011, MNRAS, 415, 3750

Moster B. P., Macciò A. V., Somerville R. S., Naab T., Cox T. J., 2012, MNRAS, 423, 2045

Murante G., Borgani S., Brunino R., Cha S.-H., 2011, MNRAS, 417, 136

Navarro J. F., Frenk C. S., White S. D. M., 1997, ApJ, 490, 493

Nelson A. F., Wetzstein M., Naab T., 2009, ApJS, 184, 326

Nelson D., Vogelsberger M., Genel S., Sijacki D., Kereš D.,

Springel V., Hernquist L., 2013, MNRAS, 429, 3353

Ostriker J. P., McKee C. F., 1988, Reviews of Modern Physics, 60, 1

Power C., Read J. I., Hobbs A., 2013, ArXiv e-prints

Price D. J., 2007, PASA, 24, 159

Price D. J., 2008, Journal of Computational Physics, 227, 10040

Price D. J., 2012, Journal of Computational Physics, 231, 759

Read J. I., Hayfield T., 2012, MNRAS, 422, 3037

Read J. I., Hayfield T., Agertz O., 2010, MNRAS, 405, 1513

Ritchie B. W., Thomas P. A., 2001, MNRAS, 323, 743

Saitoh T. R., Makino J., 2009, ApJL, 697, L99

Saitoh T. R., Makino J., 2013, ApJ, 768, 44

Sales L. V., Navarro J. F., Schaye J., Dalla Vecchia C., Springel V., Booth C. M., 2010, MNRAS, 409, 1541

Scannapieco C., Tissera P. B., White S. D. M., Springel V., 2006, MNRAS, 371, 1125

Scannapieco C. et al., 2012, MNRAS, 423, 1726

Sedov L. I., 1959, Similarity and Dimensional Methods in Mechanics

Sijacki D., Vogelsberger M., Kereš D., Springel V., Hernquist L., 2012, MNRAS, 424, 2999

Sod G. A., 1978, Journal of Computational Physics, 27, 1

Springel V., 2005, MNRAS, 364, 1105

Springel V., 2010a, MNRAS, 401, 791

Springel V., 2010b, ARA&A, 48, 391

Springel V., Di Matteo T., Hernquist L., 2005, MNRAS, 361, 776

Teyssier R., 2002, A&A, 385, 337

Valdarnini R., 2012, A&A, 546, A45

Wadsley J. W., Veeravalli G., Couchman H. M. P., 2008, MNRAS, 387, 427

Wetzstein M., Nelson A. F., Naab T., Burkert A., 2009, ApJS, 184, 298

Wiersma R. P. C., Schaye J., Smith B. D., 2009, MNRAS, 393, 99

APPENDIX A: HIGH ORDER ESTIMATE OF THE VELOCITY GRADIENT

While we use a low order estimate of the pressure gradient in the equation of motion (so as to keep the exact conservation), we are free to use a high order estimate for the velocity gradient without any trade-off in accuracy. Here, we follow the approach of Price (2012), which is equivalent to Cullen & Dehnen (2010) though with a slightly different derivation. The Greek letters (α, β, γ) stand for the coordinate index and the Roman letters are particle labels.

The commonly used estimate of the velocity gradient is

$$(\widehat{\nabla \otimes \mathbf{v}})_{\alpha\beta} = \frac{1}{\rho_i} \sum_j m_j (\mathbf{v}_j - \mathbf{v}_i)^\beta \nabla_i^\alpha W_{ij}. \tag{A1}$$

Expanding v_j^β around i:

$$v_j^\beta = v_i^\beta + \partial_\gamma v_i^\beta (\mathbf{x}_j - \mathbf{x}_i)^\gamma + O(h^2). \tag{A2}$$

Substituting into (A1) leads to

$$\sum_j m_j (\mathbf{v}_j - \mathbf{v}_i)^\beta \nabla_i^\alpha W_{ij} = \partial_\gamma v_i^\beta \sum_j m_j (\mathbf{x}_j - \mathbf{x}_i)^\gamma \nabla_i^\alpha W_{ij}. \tag{A3}$$

We can obtain the improved estimate $\partial_\gamma v_i^\beta$ from a matrix inversion $\mathbf{X} = \mathbf{M}^{-1} \mathbf{Y}$ where $\mathbf{X}_{\gamma\beta} \equiv \partial_\gamma v_i^\beta$ and

$$\begin{aligned}
\mathbf{M}_{\alpha\gamma} &\equiv \sum_j m_j (\mathbf{x}_j - \mathbf{x}_i)^\gamma \nabla_i^\alpha W_{ij} \\
&= \sum_j m_j (\mathbf{x}_j - \mathbf{x}_i)^\gamma (\mathbf{x}_i - \mathbf{x}_j)^\alpha \frac{1}{x_{ij}} \frac{\partial W_{ij}}{\partial x_{ij}},
\end{aligned} \tag{A4}$$

$$\begin{aligned}
\mathbf{Y}_{\alpha\beta} &\equiv \sum_j m_j (\mathbf{v}_j - \mathbf{v}_i)^\beta \nabla_i^\alpha W_{ij} \\
&= \sum_j m_j (\mathbf{v}_j - \mathbf{v}_i)^\beta (\mathbf{x}_i - \mathbf{x}_j)^\alpha \frac{1}{x_{ij}} \frac{\partial W_{ij}}{\partial x_{ij}}.
\end{aligned} \tag{A5}$$

The velocity divergence, shear tensor, and vorticity can be obtained readily from the velocity gradient:

$$\nabla \cdot \mathbf{v} = \partial_\alpha v^\alpha \tag{A6}$$

$$\mathbf{S}_{\alpha\beta} = \frac{1}{2}(\partial_\alpha v^\beta + \partial_\beta v^\alpha) - \frac{1}{3}\nabla \cdot \mathbf{v}\delta_{\alpha\beta} \tag{A7}$$

$$(\nabla \times \mathbf{v})_\gamma = \epsilon_{\alpha\beta\gamma}\partial_\alpha v^\beta. \tag{A8}$$